Title: Single-molecule diffusion-based estimation of GPCR activity

Authors: Masataka Yanagawa[1], Michio Hiroshima[1,2,3], Yuichi Togashi[4], Takahiro Yamashita[5], Yoshinori Shichida[5,6], Masayuki Murata[7], Masahiro Ueda[2,8], and Yasushi Sako[1,*]

Affiliations:

[1] Cellular Informatics Laboratory, RIKEN, 2-1 Hirosawa, Wako, Saitama 351-0198, Japan.

[2] Laboratory for Cell Signaling Dynamics, RIKEN Quantitative Biology Center (QBiC), 6-2-3, Furuedai, Suita, Osaka 565-0874, Japan.

[3] Japan Science and Technology Agency (JST), CREST, Saitama, Japan.

[4] Research Center for the Mathematics on Chromatin Live Dynamics (RcMcD), Hiroshima University, 1-3-1 Kagamiyama, Higashi-Hiroshima, Hiroshima 739-8526, Japan.

[5] Department of Biophysics, Graduate School of Science, Kyoto University, Kyoto 606-8502, Japan.

[6] Research Organization of Science and Technology, Ritsumeikan University. Kusatsu, Shiga 525-8577, Japan.

[7] Department of Life Sciences, Graduate School of Arts and Sciences, The University of Tokyo, Komaba 3-8-1, Meguro-ku, Tokyo 153-8902, Japan.

[8] Laboratory of Single Molecule Biology, Graduate School of Frontier Biosciences, Osaka University, 1-3 Yamadaoka, Suita, Osaka 565-0871, Japan.

*To whom correspondence should be addressed: sako@riken.jp

One Sentence Summary: Single-molecule imaging for evaluating GPCR activity by monitoring the diffusion dynamics on the cell surface.

Abstract: G protein-coupled receptors (GPCRs) are major drug targets and have high potential for drug discovery. The development of a method for measuring the activities of GPCRs is essential for pharmacology and drug screening. However, it is difficult to measure the effects of a drug by monitoring the receptor on the cell surface, and changes in the concentrations of downstream signaling molecules, which are specific to each receptor, are used as an index of the receptor activity. Here, we show that single-molecule imaging analysis provides an alternative method for assessing GPCR activity. We monitored the dynamics of the diffusion of metabotropic glutamate receptor 3 (mGluR3), a class C GPCR, under various ligand conditions by using total internal reflection fluorescence microscopy (TIRFM). The single-molecule tracking analysis demonstrate that changes in the average diffusion coefficient of mGluR3 quantitatively reflect the ligand-dependent activity. Then, we reveal that the diffusion of receptor molecules is altered by the common physiological events associated with GPCRs, including G protein binding or accumulation in clathrin-coated pits, by inhibitor assay and dual-color single-molecule imaging analysis. We also confirm the general applicability of the method to class A and B GPCRs, demonstrating that the diffusion coefficient is a good index for estimating the activities of many GPCRs regardless of the phylogenetic groups, chemical properties of the ligands, and G protein-coupling selectivity.

Introduction

G protein-coupled receptors (GPCRs) constitute the largest superfamily of human membrane proteins, and are classified into several families based on their sequence similarity (*1, 2*). About 33% of all small-molecule drugs target just 6% of the ~800 human GPCRs (*3, 4*); thus, GPCRs have immense potential for drug discovery. However, it is difficult to measure the effects of a drug by monitoring the receptor on the cell surface, and changes in the concentrations of downstream signaling molecules, including second messengers, are monitored as an index of the receptor activity (*5*). These conventional methods require background knowledge about the signaling pathways, including coupling specificity to G protein subtypes. Here, we developed an alternative method for assessing the activity of GPCRs by monitoring the movements of receptor molecules on living cells under a microscope.

Total internal reflection fluorescence microscopy (TIRFM) is a common imaging method for observing single molecules on the basal membrane of a living cell (*6-8*). Dimerization and diffusion of the M1 muscarinic receptor (*9*) and the *N*-formyl-peptide receptor (*10*) have been measured by TIRFM, but there was limited information about the activation process because the fluorescent dyes were conjugated with agonists in these studies, preventing observation of the inactive state. Recent studies have reported that the oligomerization and diffusion of the β-adrenergic receptor (*11*), $GABA_B$ receptors (*11*), and dopamine D_2 receptors (*12*) change upon ligand stimulation; however, the physiological background and generality of these observations are unknown.

Here, we examined the relationship between the diffusion and activity of metabotropic glutamate receptor 3 (mGluR3) as a model class C GPCR. Class C GPCRs have a large extracellular ligand-binding domain (ECD) on the N-terminal side of the seven alpha-helical transmembrane domains (TMDs) (Fig. 1A). The ECDs function as an obligatory dimer, where dimeric reorientation occurs upon ligand binding (*13, 14*). The conformational change in ECDs promotes the dimeric rearrangement of TMDs (*15-17*), activating a protomer of the TMD dimer (*18, 19*). Single-molecule tracking (SMT) analysis demonstrated that the average diffusion coefficient (D_{Av}) of mGluR3 quantitatively reflects receptor activity. The inhibitor assay and dual-color TIRFM analysis indicated that the slowing of mGluR3 was related to the decoupling of the receptor/G protein coupling complex followed by the receptors accumulating in clathrin-coated pits (CCPs). We verified the generality of the agonist-induced change in the diffusion dynamics of GPCRs by comparing the D_{Av} of nine GPCRs in various phylogenetic positions.

Results

Expression, fluorescence labeling, single-molecule imaging, and MSD-Δt plot analysis of HaloTag fusion mGluR3

To determine the relationship between the diffusion coefficient and activity of mGluR3, we monitored the single-molecule movement of TMR-labeled HaloTag fusion mGluR3 on HEK293 cells under various ligand conditions (Fig. 1, Movie 1). The fusion of HaloTag to the C-terminus of mGluR3 did not alter the dimerization, ligand binding, and G protein activation (Fig. S1). In the single-molecule imaging, ~95% of the HaloTag-fused mGluR3 molecules were labeled with TMR ligands with low non-specific binding (Fig. S2A, B). Because HEK293 cells express no detectable mRNA for

mGluRs (*20*), almost all receptor molecules were labeled in the present measurements. The mean density of receptor molecules on a cell surface was 0.40 ± 0.11 particles/μm^2 in the single-molecule images (Fig. S2C; mean ± SD).

We quantified the mean square displacement (MSD) from the trajectories traced by SMT in each cell (Fig. 1B), and analyzed the dose-dependent change in the total average MSDs of the trajectories (Fig. 1C–E). Stimulation with the inverse agonist LY341495 significantly increased the MSD of mGluR3 molecules (Fig. 1C). In contrast, stimulation with the agonist LY379268 significantly decreased the MSD in a dose-dependent manner (Fig. 1D). We also analyzed the LY379268-dependent diffusion change of mGluR3 in the presence of 1 μM MNI137, a negative allosteric modulator (NAM) (*21*). MNI137 binding to the TMD suppressed the agonist-dependent decrease of MSD, and no significant difference was observed upon LY379268 stimulation (Fig. 1E).

Relationship among average diffusion coefficient, ligand binding affinity, and G protein activation efficiency of mGluR3

We calculated the D_{Av} of mGluR3 molecules from the MSD (equations 1 and 2 in Methods). The dose-dependent curves showed the LY341495-induced increase and LY379268-induced decrease of D_{Av} in the absence of other ligands (Fig. 2A). The LY379268-dependent decrease of D_{Av} was greater in the presence of 100 nM LY341495, and was significantly suppressed by the addition of 1 μM MNI137 (Fig. 2B). To compare the dose-dependency of D_{Av} with the ligand-binding affinity of mGluR3, we performed an *in vitro* [^{3}H]-LY341495 binding assay (Fig. 2C, D). The EC_{50} value of the LY341495-induced increase of D_{Av} (Fig. 2A) was at most half that of [^{3}H]-LY341495 binding (Fig. 2C). The IC_{50} values of the LY379268-induced decrease of D_{Av} without and with 100 nM LY341495 (Fig. 2A, B) were at most twice that of the competition binding curve between LY379268 and 100 nM [^{3}H]-LY341495 (Fig. 2C). These results suggested that the dose-dependency of D_{Av} corresponded well with the ligand-binding affinity. The effect of MNI137 on mGluR3 could not be measured by the [^{3}H]-LY341495 binding assay; no significant difference was observed with and without 1 μM MNI137 (Fig. 2D).

We also measured the G protein activation efficiencies of mGluR3 under the same ligand conditions with an *in vitro* [^{35}S]-GTPγS binding assay. mGluR3 showed a high G protein activation even without ligands, and this basal activity was suppressed by LY341495 in a concentration-dependent manner (Fig. 2E). This is consistent with a recent study demonstrating that Cl^- binding to the ECD causes high basal activity of

mGluR3 (*22, 23*). Thus, the inverse agonist-induced increase and agonist-induced decrease of D_{Av} in Fig. 2A reflected the change in the equilibrium between the inactive and active states of mGluR3 molecules on the cell surface. Furthermore, 1 μM MNI137 significantly suppressed the agonist-induced increase of G protein activation efficiency (Fig. 2F), as expected from D_{Av} of mGluR3 (Fig. 2B).

The IC_{50} of LY341495-induced suppression of the basal activity (Fig. 2E) was one order of magnitude smaller than those obtained from the ligand-binding assay (Fig. 2C) and from the dose-dependency of D_{Av} (Fig. 2A). Furthermore, there was a difference of two orders of magnitude between the EC_{50} values of the LY379268-dependent increase of G protein activation efficiencies with (Fig. 2F) and without 100 nM LY341495 (Fig. 2E), where that with 100 nM LY341495 was similar to those estimated from the ligand binding assay (Fig. 2C) and from the dose-dependency of D_{Av} (Fig. 2A, B). Generally, it is difficult to estimate the ligand occupancy from a downstream response after amplification of the signaling cascade because the response is usually saturated at a ligand concentration lower than the saturation binding (*24*). Single-molecule imaging analysis allows us to assess the fraction of receptors in the inactive and active states, which corresponds well to the fraction of ligand binding. Under ligand saturation conditions, changes in D_{Av} and G protein activation efficiency were consistent (Fig. 2G).

Ligand-induced changes in the mGluR3 diffusion state distribution

Next, we performed variational Bayesian-hidden Markov model (VB-HMM) clustering analysis (*25, 26*) to classify the diffusion states of mGluR3. VB-HMM analysis of the total trajectories suggested that the diffusion of mGluR3 molecules could be classified into four states (immobile, slow, medium, fast) (Figs. 3A, B, S3, and Movie 1). The fast and medium states contained transient directional and non-directional movements and their MSD-Δt plots were linear in the average (Fig. S3C, D). In contrast, concave-down MSD-Δt plots were observed in the slow and immobile states (Fig. S3E, F), indicating the confined diffusion of mGluR3 (*27*). The confinement lengths were estimated to be 140 and 70 nm, respectively (Fig. S3E, F, and Methods), which were consistent with the radii of plasma membrane microdomains (*28*). The distribution of the apparent oligomer size of mGluR3 in each diffusion state was estimated from the intensity histogram based on the sum of Gaussian functions. The mean intensity of monomeric TMR estimated from the intensity histogram of TMR-labeled CD86, a monomeric membrane protein, on HEK293 cells (*11*) (Fig. S3G), was about half of that of the highest peak in the histogram of mGluR, suggesting that the

majority of mGluR forms dimers (Fig. S3H). The higher-order clusters of mGluR3 were mainly related to the immobile state, where the intensity histogram was right-shifted compared with the other diffusion states (Fig. S3H).

Upon LY341495 stimulation, the fraction of fast state molecules significantly increased, whereas the fractions of immobile and slow state molecules decreased in a dose-dependent manner (Fig. 3C). In contrast, LY379268 stimulation increased the fraction of the immobile and slow states, but decreased the fraction of the fast state (Fig. 3D). To analyze the transitions among the four states, we estimated the time constants of the state transition from the VB-HMM transition array (Figs. 3E, S4). The dose-dependent changes were mainly observed in the transition from the slower to the faster states, suggesting that the activation of mGluR3 made it difficult to escape from the microdomain and that mGluR3 was trapped in a slower state. The diffusion coefficients of medium and slow states estimated from the VB-HMM analysis also changed significantly upon ligand stimulation (Figs. 3E, S5). The ligand-induced changes in D_{Av} in Fig. 2A, B were derived from the opposite change in the fraction of the fast state compared with the slow and immobile states, and also from the changes in the diffusion coefficients in the medium and slow states (Fig. 3E).

Effects of pertussis toxin on mGluR3 molecule diffusion

We analyzed the effect of pertussis toxin (PTX), an inhibitor of $G_{i/o}$ proteins, to link the diffusion state with the G protein-bound state of mGluR3 (Fig. 4A). The PTX treatment decreased the average diffusion coefficient significantly (Fig. 4B, C), reflecting a decrease in the fast state fraction and an increase in the immobile state fraction for the inactive (100 nM LY341495) and active (100 μM LY379268) ligand conditions, respectively (Fig. 4F, G). To confirm that the effect of PTX was caused by the loss of the interaction between mGluR3 and $G_{i/o}$, we analyzed the effects of the B oligomer of PTX as a negative control. The B oligomer carries the A protomer that catalyzes ADP-ribosylation of the $G_{i/o}$ α-subunit (*29*) (Fig. 4A). Treatment with the B oligomer alone did not alter the diffusion of mGluR3 (Fig. 4D–G), indicating that the ADP-ribosylation of the $G_{i/o}$ α-subunit by the A protomer was responsible for the slowing of mGluR3. These results suggest that the fast diffusion state contained $G_{i/o}$ protein-bound mGluR3 for both the inactive and active ligand conditions. This is consistent with previous studies, which demonstrated precoupling of GPCRs with G protein even in the inactive state, enabling fast signal transduction (*30-32*). The activation of mGluR3 triggered a release of $G_{i/o}$ from the precoupling complex, similar to PTX-induced decoupling (Fig. 4A), thereby decreasing the fast state fraction. Thus,

the decrease in D_{Av} upon agonist stimulation in Fig. 2A, B is partly explained by the decrease in mGluR3 coupling with $G_{i/o}$ protein.

Dual-color TIRFM analysis of mGluR3 colocalized with clathrin

We investigated the physiological events related to the immobile state that increased upon activation of mGluR3, in contrast to the decrease in the fast state. A TIRFM image showed that the immobile state was related to clustering of mGluR3 molecules followed by internalization (Fig. 5A). Immobile clusters of mGluR3 were formed and disappeared with rapid directional movement (Movie 2). To test whether the clusters were receptors in the CCP, we analyzed the colocalization of TMR-labeled mGluR3 and green fluorescent protein (GFP)-labeled clathrin light chain (CLC) by dual-color TIRFM. When mGluR3 and CLC were colocalized, TMR intensity increased rapidly (Fig. 5B, C, and Movie 3). The intensities of TMR and GFP decreased simultaneously several seconds after colocalization (Fig. 5C). These results suggested that mGluR3 formed a large cluster in a CCP and the cluster was internalized as a clathrin-coated vesicle in the cytoplasmic region, which could not be reached by the evanescent light (Fig. 5A).

Next, we quantified the distribution of the diffusion states of mGluR3 colocalized with CLC (mGluR3/CLC) and compared it with the total number of mGluR3 molecules (mGluR3/total) for the inactive (100 nM LY341495) and active (100 μM LY379268) ligand conditions. The immobile state fraction was significantly higher in mGluR3/CLC than in mGluR3/total, indicating that the clathrin binding immobilized the receptor (blue and red lines, Fig. 5D). Comparing the inactive and active ligand conditions demonstrated that the fraction of the immobile state of mGluR3/CLC increased upon activation (black lines, Fig. 5D). Furthermore, the probability and time constant of the colocalization between mGluR3 and CLC were increased significantly after activation (Fig. 5E–G). The cumulative histogram of the colocalization duration was fitted with a double exponential function with short and long time constants (Fig. 5F). The short component of colocalization may include the mGluR3 incidentally adjacent to CLC, where no significant difference was observed between LY341495 and LY379268 (Fig. 5G). In contrast, the time constant of the long component for the active ligand conditions was ~2-fold longer than that of the inactive ligand conditions (Fig. 5G). Because the ratio of short to long components was not changed by activation (inset, Fig. 5G), the ~1.6-fold increase in the probability of colocalization in Fig. 5E was mainly caused by the increase of the colocalization duration. Thus, the immobile state fraction

in the total trajectories reflected the number of mGluR3 molecules interacting with clathrin molecules, which increased upon activation.

Correlation between receptor density, mean oligomer size, and D_{Av}

We also analyzed the ligand-induced changes in mean oligomer size, which should be related to internalization. However, the mean oligomer size showed no clear dose-dependency (Fig. S6A–C). This may be due to the higher correlation between mean oligomer size and receptor density (Fig. S6D–G). The mean oligomer size of mGluR3 was significantly and positively correlated with receptor density (Fig. S6G). Thus, the strict selection of cells based on receptor density is required to test the ligand effect on oligomer size. In contrast, no significant correlation was observed between receptor density and D_{Av} (Fig. S7). D_{Av} is a robust index of mGluR3 activity that is independent of the receptor expression level.

Generality of the agonist-induced diffusion change of GPCRs

To test the generality of the relationship between the diffusion and activation of GPCRs, we monitored the single-molecule movement of fluorescently labeled GPCRs in other classes (Table 1, Movie 4). Because it is not necessary to label all the molecules in a cell to measure D_{Av}, we used 30 nM STELLA Fluor 650 (SF650) HaloTag as a ligand for labeling to improve the quality of the single-molecule imaging. SF650 is a bright, stable fluorescence dye with a 4-fold higher affinity for HaloTag than the TMR ligand (Fig. S2B, D). Under the labeling conditions, ~70% of receptors were labeled with SF650 with lower non-specific binding (Fig. S2D).

We compared the MSD-Δt plots of the trajectories of GPCR molecules with and without agonist stimulation (Fig. S8), and calculated D_{Av} as listed in Table 1. All the GPCRs tested showed significant slowing upon agonist stimulation regardless of the phylogenetic positions, chemical properties of the ligands, and G protein-coupling selectivity (Table 1, Fig. S8). In the absence of ligands, mGluR3 showed lower D_{Av} (0.047 $\mu m^2/s$) than other GPCRs (0.06–0.09 $\mu m^2/s$), which corresponded to that of mGluR3 with 1 μM LY341495 (0.064 $\mu m^2/s$) (Table 1). Thus, the diffusion coefficient of mGluR3 was similar to those of other GPCRs in the inactive state (Fig. 2E). In the presence of an agonist, the D_{Av} of GPCRs was 0.04–0.07 $\mu m^2/s$. A drug effect on each GPCR was accurately detected by SMT analysis as a change in D_{Av} (Table 1), but the absolute values of D_{Av} varied between GPCRs.

Discussion

The present study provides a new method for assessing the effects of drugs on GPCRs by monitoring the diffusion behavior of GPCRs. We obtained proof-of-concept of the applicability of single-molecule imaging to the pharmacology of a class C GPCR, mGluR3. The basal activity, agonist-induced activation, inverse agonist-induced inactivation, and NAM-dependent suppression of activity can be evaluated by measuring D_{Av} of mGluR3 on the living cell surface (Fig. 2). The dose-dependent change of D_{Av} was derived from the population shift of the four diffusion states and the change of the diffusion coefficient of each state (Fig. 3E).

The PTX treatment assay suggested that the fast state is related to the mGluR3 binding with the G protein (Fig. 4). Before the experiment, we expected that PTX would have an effect only under the active ligand conditions; however, this was not the case. The slowing of the mGluR3 by PTX was observed more clearly under the inactive ligand conditions (Fig. 4), providing evidence of mGluR3/G protein precoupling. Precoupling of GPCRs with G proteins has been demonstrated in class A GPCRs (*30-32*). A larger PTX-induced decrease in the fast state in the presence of LY341495 than in the presence of LY379268 (Fig. 4F, G) is consistent with the previous model in which the precoupled state is more stable than the active ternary complex (*30*). It is currently unknown why G protein binding accelerates the diffusion of mGluR3. A previous report revealed that hopping over the diffusion barrier was controlled by an interaction between the C-terminal region of mGluR5 and a cytosolic partner in astrocytes (*33*). The receptor/G protein precoupling, where the C-terminal region of GPCR also plays an essential role (*32*), would affect the ability to cross the membrane microdomain for a similar reason.

The recruitment of GPCRs into CCPs is also a well-established mechanism for endocytosis regardless of the GPCR family. The dual-color TIRFM analysis demonstrated that the immobile state of mGluR3 is related to the interaction with clathrin molecules (Fig. 5). During desensitization, GPCRs are phosphorylated by G protein-coupled receptor kinases, followed by the recruitment of arrestins (*34*). Then, the GPCR/arrestin complexes are gathered into CCPs through the interactions between arrestin, clathrin, and the AP2 adaptor (*34*). Previously, the clathrin-mediated endocytosis of class A GPCRs, including adrenergic and opioid receptors, was analyzed by TIRFM under high-expression conditions where a single receptor molecule could not be resolved, and it was demonstrated that the GPCR cargo regulates the surface residence time of CCPs (*35, 36*). The present results indicate that the time constant of colocalization between mGluR3 and CLC molecules increases upon agonist stimulation

(Fig. 5F, G), which is qualitatively consistent with these previous reports. The absolute values of the colocalization time constant were two orders of magnitude shorter than the previously reported values for bulk imaging, and is probably due to the higher photobleaching rate of single TMR ligands (~3 s) in single-molecule imaging. Thus, it is rare to observe the whole process, from the recruitment of receptors into the CCP to the internalization, as shown in Fig. 5B, C, where the clustering rate of the receptor-clathrin complex was greater than the photobleaching rate.

These physiological events, which affect diffusion, are not specific to class C GPCRs. If a drug effect on a GPCR can be estimated from a common change in the diffusion dynamics, we could perform drug assessments of GPCRs without knowing the specific signaling cascade. Therefore, we verified the generality of the diffusion change upon activation in various GPCRs in other classes. Comparison of the diffusion coefficients of GPCRs with and without an agonist demonstrated that the slowing of receptor diffusion upon activation is a general feature of GPCRs irrespective of the signaling pathways downstream of the receptor (Table 1, Fig. S8).

The agonist-induced increases of diffusion coefficients of $GABA_B$ (*11*) and dopamine D_2 receptors (*12*) were reported in previous studies. The apparent discrepancy between the present study and the previous studies arose from the labeling methods used in each study. In the previous studies, N-terminally SNAP-tagged GPCRs were labeled with non-membrane-permeable fluorophores (*11, 12*). In this method, only the receptor molecules on the cell surface were labeled at some time point, similar to a pulse-chase experiment. Therefore, the agonist-induced internalization of receptors caused the selective loss of the immobilized receptors in CCPs from the measurements. In contrast, we used membrane-permeable fluorophores, which allowed us to uniformly label the receptor molecules in the cell. The whole-cell labeling allowed us to monitor the total number of receptor molecules at steady state, with or without ligands on the cell surface, including newly exocytosed receptors after labeling. Furthermore, there is a clear difference between the analysis in the present study and that used in the study by Tabor et al., (*12*) who excluded slow-moving receptors ($D < 0.02$ $\mu m^2/s$). If we performed a similar analysis here, the immobile and slow diffusion fractions of mGluR3 would be almost completely filtered out, resulting in a misleading evaluation of D_{Av}.

In conclusion, the diffusion coefficient is a good index for estimating the activities of various GPCRs on a living cell. The present method can be applied to HEK293 cells transiently expressing fluorescently labeled GPCRs because D_{Av} is hardly affected by variability in the cell surface receptor density (Fig. S7). Because it is possible to quantify the diffusion of any GPCR by using TIRFM, our technique could

be useful for drug screening of many GPCRs, including orphan GPCRs, about which little is known. We anticipate that the present study will contribute to the future development of a single-molecule dynamics-based pharmacological method for GPCRs.

Materials and Methods

Materials

[^{3}H]-LY341495 (1.28 TBq/mmol), LY341495, LY379268, NMI137, and NECA, serotonin were purchased from Tocris Cookson. Isoproterenol, histamine, DHA, CXCL12, TRAP-6, and glucagon were purchased from Santa Cruz, Wako, Sigma Aldrich, Thermo Fisher, BACHEM, and CEDARLANE, respectively. [^{35}S]-GTPγS (37 TBq/mmol) was purchased from PerkinElmer Life Sciences. PTX and B oligomer were purchased from Wako Chemicals. Human CD86 cDNA was purchased from OriGene.

Construction of cDNA

The HaloTag7 (Promega) coding sequence was amplified by PCR, and was fused at the C-terminus of mouse mGluR3 with an In-Fusion HD Cloning Kit (Clontech). To quantify the expression of wild type and HaloTag-fused mGluR3 by Western blotting analysis, the epitope sequence of the anti-bovine rhodopsin monoclonal antibody Rho1D4 was also fused at the C-terminus. The cDNAs of mGluR3s were introduced into the pcDNA3.1 mammalian expression vector (Invitrogen). The cDNAs of other GPCRs (ADRB2, HTR2A, HRH1, ADORA2A, FFAR4, CXCR4, F2R, GCGR) were purchased from Promega, and the receptor coding sequences were inserted into pFC14K HaloTag CMV Flexi Vector. The CD86 (M1-R277) coding sequence was amplified by PCR, and inserted into the pEGFP-N1 mammalian expression vector (Clontech), where the coding sequence of EGFP was swapped with that of HaloTag7. The cDNA of GFP-tagged CLC was constructed as previously reported (*37*).

Single-molecule imaging

HEK293 cells were cultured in DMEM/F12 containing phenol red (Gibco) supplemented with 15 mM HEPES (pH 7.3), 29 mM $NaHCO_3$, and 10% FBS at 37 °C under 5% CO_2. The plasmid DNA of HaloTag-fused mGluR3 was transfected into HEK293 cells cultured on glass coverslips (Matsunami) on a 60-mm dish 1 day before imaging. Lipofectamine 3000 (Invitrogen) was used for transfection. After 15 min

incubation at room temperature, the transfection mixture (plasmid DNA (0.1 μg), P3000 reagent (0.2 μL), Lipofectamine 3000 reagent (2.5 μL), and Opti-MEM (120 μL, Gibco)) was added to cells cultured with DMEM/F12 (3 mL) on a 60-mm dish. For dual-color imaging, the plasmid DNA of GFP-fused CLC (0.02 μg) was co-transfected with HaloTag-fused mGluR3. After 3 h incubation at 37 °C under 5% CO_2, the medium was changed to DMEM/F12 without phenol red (3 mL, Gibco) supplemented with 10% FBS.

After overnight incubation, the HaloTag-fused mGluR3 was labeled with 300 nM HaloTag TMR ligand (Promega) in DMEM/F12 without phenol red for 15 min at 37 °C under 5% CO_2. For imaging of other GPCRs, we used 30 nM SF650 HaloTag ligand (GORYO Chemical). The HaloTag ligand-treated HEK293 cells on coverslips were washed three times with DMEM/F12 without phenol red (3 mL) in a 60-mm dish. For the inhibitor assay, the cells were treated with 5 nM PTX, 5 nM B oligomer, or vehicle for 6 h at 37 °C under 5% CO_2 before imaging. Cells were washed twice with PBS and DMEM/F12 without FBS before HaloTag ligand treatment.

The coverslip was mounted on a metal chamber (Invitrogen), and washed five times with Hanks' balanced salt solution (HBSS; 400 μL, Sigma); with 15 mM HEPES (pH 7.3) and 0.01% BSA, without $NaHCO_3$). Ligand (5× concentration) or vehicle solution (100 μL) was added to the chamber with 0.01% BSA/HBSS (400 μL) 10 min before imaging. Single-molecule imaging was performed 10–30 min after ligand (or vehicle) stimulation at room temperature (25 °C). The fluorescently-labeled GPCRs on the basal cell membrane were observed with total internal reflection illumination by using an inverted fluorescence microscope (TE2000, Nikon). The cells were illuminated with a 559 nm, 100 mW laser (WS-0559-050, NTT Electronic) for TMR, with a 488 nm, 200 mW laser (Sapphire 488-200, Coherent) for GFP, or with a 637 nm, 140 mW laser (OBIS 637, Coherent) through the objective (PlanApo 60×, NA 1.49, Nikon) by a dichroic mirror (FF493/574, Semrock) for TMR and GFP, or by a single-band filter set (ET Cy5, Chroma) for STELLA Fluo 650. The emission light from TMR and GFP was split into two light paths by a two-channel imaging system (M202J, Nikon) with a dichroic mirror (59004b, Chroma) and simultaneously detected by two EM-CCD cameras (ImagEM, Hamamatsu) after passing through band-pass filters (ET525/50m for GFP, ET605/70m for TMR, Chroma). The 4× relay lens was placed before the two-channel imaging system to magnify the image (67 nm/pixel). The fluorescence images were recorded with image software (ImagEM HDR, Hamamatsu) with the following settings: exposure time, 30.5 ms; electron multiplying gain, 200; spot noise reduction, on. The cells were fixed to evaluate the accuracies of the positions of TMR-labeled

mGluR3, and GFP-labeled CLC was performed according to a previous method (*38*). The cells on a coverslip were treated with 4% paraformaldehyde/0.2% glutaraldehyde in PBS for 30 min at room temperature, and they were washed five times with HBSS before imaging.

Analysis of single-molecule images

The multiple TIFF files (16 bit) were processed by ImageJ as follows. Background subtraction was performed with a rolling ball radius of 25 pixels, and two-frame averaging of the images was then conducted by the Running_ZProjector plugin (Vale Lab homepage, http://valelab.ucsf.edu/~nstuurman/ijplugins/). The dual-color images were aligned by the GridAligner plugin (Vale Lab homepage) based on an affine transform algorithm. The two channels were calibrated with scattering images of gold particles (60 nm) recorded on the same day. To keep the single-molecule intensity constant across the images, the display range of the brightness and contrast was set as a constant range (minimum: 0, maximum: 1800) followed by image conversion to avi format (8 bit) without compression. SMT analysis was performed with G-count software (G-angstrom) based on a two-dimensional Gaussian fitting algorithm with the following parameters: region of interest size, 6 pixels; Fluorescence limit, 12 arbitrary units; loop, seven times; minimum of 15 frames.

The calculation of the parameters from trajectories, the curve fittings, and the illustrations in the Figures were obtained with Igor Pro 6.36 (WaveMetrix) as follows. The MSD within time $n\Delta t$ of each trajectory was calculated by (*27*)

$$\mathrm{MSD}(\mathrm{n}\Delta\mathrm{t}) = \frac{1}{\mathrm{N}-1-\mathrm{n}} \sum_{j=1}^{N-1-n} [\{x(j\Delta\mathrm{t}+\mathrm{n}\Delta\mathrm{t}) - \mathrm{x}(j\Delta\mathrm{t})\}^2 + \{y(j\Delta\mathrm{t}+\mathrm{n}\Delta\mathrm{t}) - \mathrm{y}(j\Delta\mathrm{t})\}^2] \quad (1)$$

where n is the length of frames, Δt is the frame rate (30.5 ms), and N is the total frame number of the trajectory. D_{Av} was calculated based on the two-dimensional diffusion equation

$$D_{Av}(\mathrm{n}\Delta\mathrm{t}) = \frac{1}{\mathrm{M}} \sum_{j=1}^{M} \frac{MSD_j(\mathrm{n}\Delta\mathrm{t})}{4\mathrm{n}\Delta\mathrm{t}} \quad (2)$$

where MSDj is the MSD of the j-th trajectory and M is the total number of trajectories. D_{Av} in the present study was calculated for $n = 6$ ($n\Delta t = 183$ ms). The EC_{50} and IC_{50} of the ligand-dependent changes of D_{Av} were calculated by equations 3 and 4, respectively.

$$f(x) = \text{bottom} + \frac{\text{top} - \text{bottom}}{1 + \frac{EC_{50}}{x}} \quad (3),$$

$$f(x) = \text{top} + \frac{\text{bottom} - \text{top}}{1 + \frac{IC_{50}}{x}} \quad (4).$$

The MSD-Δ*t* plot was fitted by(*39*)

$$\text{MSD}(\Delta t) = \frac{L^2}{3}\left(1 - \exp\left(\frac{-12D\Delta t}{L^2}\right)\right) \quad (5)$$

where *L* is the confinement length and *D* is the diffusion coefficient taking the limit of Δ*t* to 0.

The histogram of the displacement ($r = \sqrt{\text{MSD}}$) within Δ*t* (30.5 ms) of the trajectories of each HMM diffusion state was fitted by (*40*)

$$P(r) = \frac{r}{2D\Delta t}\exp\left(\frac{-r^2}{4D\Delta t}\right) \quad (6)$$

.

The histogram of the intensity distribution was fitted by sum of the *N* Gaussian

$$P(x) = \sum_{n=1}^{N} A_n \exp\left(-\frac{(x - nI)^2}{2n\sigma^2}\right) \quad (7)$$

where *n* is the oligomer size, and *I* and σ are mean and SD of a single TMR molecule, respectively. *N* was determined by using the Akaike information criterion. *I* and σ were estimated to be 530 and 210 from the measurement of TMR-labeled CD86. The percentage of each oligomer size, *Percent(n)*, and mean oligomer size on each cell surface were calculated by equations 8 and 9, respectively.

$$Percent(n) = \frac{100\sqrt{2n\pi}\sigma A_n}{\sum_{n=1}^{N}\sqrt{2n\pi}\sigma A_n} \quad (8)$$

$$mean\ oligomer\ size = \sum_{n=1}^{N} \frac{n\ Percent(n)}{100} \quad (9)$$

The colocalization of TMR-labeled mGluR3 and GFP-labeled CLC was defined as particles within 100 nm of each other in the same frame. The position accuracies of TMR-labeled mGluR3 and GFP-labeled CLC on the fixed cells were estimated to be 28 and 31 nm, respectively, from 1 SD of the displacement distribution of the immobile particles. The error of the alignment between the two channels after the image processing was estimated to be 18 nm from the difference in the positions of the same gold particles. Therefore, 100 nm corresponded to ~2 SD of the total position accuracy. The time constants of colocalization were estimated from a curve fitting of the cumulative histogram (Fig. 4F) by the double exponential equation 8.

$$P(t) = A_1 \exp\left(-\frac{t}{\tau_1}\right) + A_2 \exp\left(-\frac{t}{\tau_2}\right) \quad (10)$$

The fraction of two components was estimated from the ratio of A_1 to A_2.

VB-HMM clustering analysis of trajectories of mGluR3

The VB-HMM analysis was performed with a LabView-based homemade program developed according to previously reported algorithms (*25, 26*). A trajectory of mGluR3 molecule consists of time series of step displacements. Each time series of the observed data is given as $\boldsymbol{X} = \{x_1, \ldots, x_N\}$, where N is the total number of frames. A corresponding time series of diffusion states is defined as $\boldsymbol{Z} = \{\boldsymbol{z}_1, \ldots, \boldsymbol{z}_N\}$. Here, $\boldsymbol{z}_n = \{\boldsymbol{z}_{n1}, \ldots, \boldsymbol{z}_{nK}\}$, in which K is the total number of states, and z_{nk} =1 and 0 otherwise for a molecule in the k-th state and n-th frame. In order to estimate the state series $\boldsymbol{Z}$ from the data $\boldsymbol{X}$, we applied the HMM where $\boldsymbol{Z}$ is assumed to obey the Markov process with transition matrix $\boldsymbol{A}$. The distributions of the initial state and transition probability are described as follows, respectively:

$$p(z_1 \mid \pi) = \prod_{i=1}^{K} \pi_i^{z_{1i}} \quad (11)$$

$$p(z_n \mid z_{n-1}, A) = \prod_{i=1}^{K} \prod_{j=1}^{K} A_{ij}^{z_{(n-1)i}\ z_{nj}} \quad (12)$$

where $\pi_k \equiv p(z_{1i} = 1)$ satisfies $0 \le i \le 1$ and $\sum_i \pi_i = 1$, and A_{ij} is an element of A from the i to j-th state and satisfies $0 \le A_{ij} \le 1$. The distribution of the emission probability, which represents the observation probability of the step displacement, is described with parameters ϕ as follows,

$$p(x_n|z_n,\phi) = \prod_{k=1}^{K} p(x_n|z_n,\phi)^{z_{nk}} \quad (13)$$

The probability is described with a two-dimensional diffusion equation,

$$p(x_n|z_n,D_k) = \frac{x_n}{2D_k\delta t}\exp\left(-\frac{x_n^{\ 2}}{4D_k\delta t}\right) \quad (14)$$

where D_k is the diffusion constant of state k, and δt is the frame rate (30.5 ms).

Thus, the joint probability distribution, $p(\boldsymbol{X}, \boldsymbol{Z}\,|\theta)$ is

$$p(X,Z|\theta) = p(z_1|\pi)\times\prod_{n=2}^{K} p(z_n|z_{n-1},A)\times\prod_{m=1}^{K} p(x_m|z_m,\phi) \quad (15)$$

where $\theta = \{\pi, A, \phi\}$ is the parameters of the observation probability. Molecular states Z and model parameters θ were estimated by using the VB method (*41*) to satisfy the maximum value of the logarithmic likelihood function of $p(X)$. When the distribution of θ is specified by the model M,

$$\begin{aligned}\ln p(X) &= \ln\sum_Z\int p(X,Z,\theta|M)d\theta. \\ &= \sum_Z\int q(Z,\theta)\ln\frac{q(Z,\theta)}{p(Z,\theta\,|\,X,M)}\mathrm{d}\theta + \sum_Z\int q(Z,\theta)\ln\frac{p(X,Z,\theta|M)}{q(Z,\theta)}\mathrm{d}\theta \\ &= KL(q\,||\,p) + L_q \quad (16)\end{aligned}$$

where KL($q||p$) is the Kullback-Leibler divergence between the distribution of model p and posterior function q. Because KL($q||p$) has fixed values for M and observable X, L_q corresponds to the lower bound of ln$P(X)$. When $q(\boldsymbol{Z},\theta)$ is assumed to be factorized as

$$q(Z,\theta)=q(Z)q(\theta)=q(Z)\prod_{i=1}^{I}q(\theta_i) \quad (17)$$

where I is the number of parameters. Thus, L_q can be written as,

$$L_q=\sum_{Z}\int q(Z)q(\theta)\ln\frac{p(X,Z,\theta|M)}{q(Z)}\mathrm{d}\theta-\sum_{i=1}^{I}\int q(\theta_i)\ln q(\theta_i)\,\mathrm{d}\theta_i \quad (18)$$

To optimize the distribution functions $q(Z)$ and $q(\theta)$, the variational Bayesian (VB)-EM algorithm was applied (*41*). The VB-E step and VB-M step maximize L_q against $q(Z)$ and $q(\theta)$, respectively. The VB-E step corresponds to the calculation of

$$\begin{aligned}\ln q(Z)&=E_\theta\left[\ln p(X,Z,\theta|M)\right]+const\\&=\int q(\theta)\ln p(X,Z,\theta|M)\,\mathrm{d}\theta+const \quad (19)\end{aligned}$$

where $E_\theta[...]$ means the expectation with respect to θ. Thus,

$$q(Z)\propto\exp\left\{\int q(\theta)\ln p(X,Z,\theta|M)\,\mathrm{d}\theta\right\} \quad (20)$$

By taking equation (15) into equation (20) and incorporating M,

$$q(Z)\propto\tilde{p}(z_1|\pi,M)\times\prod_{n=2}^{K}\tilde{p}(z_n|z_{n-1},A,M)\times\prod_{m=1}^{K}\tilde{p}(x_m|z_m,\phi,M) \quad (21)$$

Based on equations (11~13), each term of equation (21) becomes

$$\tilde{p}(z_1|\pi, M) = \prod_{i=1}^{K} \exp\left(\overline{\ln \pi_i}\right)^{z_{1i}} \quad (22)$$

$$\tilde{p}(z_n|z_{n-1}, A, M) = \prod_{i=1}^{K}\prod_{j=1}^{K} \exp\left(\overline{\ln A_{ij}}\right)^{z_{n-1,i}\, z_{nj}} \quad (23)$$

$$\tilde{p}(x_m|z_m, \phi, M) = \prod_{k=1}^{K} \exp\left(\overline{\ln p(x_m|z_m, \phi, M)}\right) \quad (24)$$

where the overhead lines denote averages. $q(Z)$ is optimized by the forward-backward algorithm using equations (22~24). Similarly, the VB-M step corresponds to the calculation of

$$\begin{aligned} \ln q(\theta_j) &= E_Z\left[\ln p(X, Z, \theta|M)\right] + const \\ &= \sum_Z q(Z) \int \prod_{i \neq j} q(\theta_i) \ln p(X, Z, \theta|M)\, \mathrm{d}\theta_i + const \quad (25) \end{aligned}$$

Thus,

$$q(\theta_j) \propto \exp\left\{ \sum_Z q(Z) \int \prod_{i \neq j} q(\theta_i) \ln p(X, Z, \theta|M)\, \mathrm{d}\theta_i \right\} \quad (26)$$

$q(\theta_j)$ can be factorized to separate terms for each parameter. By optimizing $q(\theta_j)$, the expectations of parameters are obtained and used as updated values in the next VB-E step.

The Dirichlet distribution was used for given prior functions of the initial state, transition probability distributions, and the calculated posterior functions. Thus, the log of expectation of the initial state is obtained as

$$\langle \ln \pi_i \rangle = \psi\left(u_i^{\pi} + \overline{z_{1,i}}\right) - \psi\left(\sum_i^K u_i^{\pi} + 1\right) \quad (27)$$

where $\Psi(x)$ is the digamma function, $\psi(x) = \frac{d}{dx} \ln \Gamma(x) = \frac{\Gamma'(x)}{\Gamma(x)}$, and u_i^{π} is the hyper parameter of the prior function and given as a flat probability distribution, $u_i^{\pi}=1$. The log of expectation of the transition probability is

$$\langle \ln A_{ij} \rangle = \psi\left(u^{A}{}_{ij} + \sum_{n=2}^{N} \overline{z_{n-1,i} z_{n,j}}\right) - \psi\left(\sum_j^K \left(u^{A}{}_{ij} + \sum_{n=2}^{N} \overline{z_{n-1,i} z_{n,j}}\right)\right) \quad (28)$$

where u^A_{ij} is the hyper parameter and u^A_{ij}=1. For the emission probability of a two-dimensional diffusion equation (equation (14)), the prior function, including the diffusion coefficient (D_k), is given by a gamma distribution, and the log-expectation of parameter τ^D_k (=1/2$D_k\delta t$) is

$$\left\langle \ln \tau^D{}_k \right\rangle = \psi\left(a_D + \sum_{n=1}^{N} \overline{z_{n,i}} \right) - \ln\left(b_D + \tfrac{1}{2} \sum_{n=1}^{N} \overline{z_{n,i}} x_n{}^2 \right) \quad (29)$$

where a_D and b_D are the hyper parameters and assigned values to maximize the lower bound L_q, which was rewritten from equation (18) as

$$L_q = E[\ln p(\pi)] + E[\ln p(A)] + E[\ln p(\phi)] - E[\ln q(\pi)] - E[\ln q(A)] - E[\ln q(\phi)] + \sum_{n=1}^{N} \ln c_n \quad (30)$$

where c_n is the scaling factor calculated in the VB-E step. The iteration between the VBE- and VBM-step is performed until the lower bound converges.

The VB-HMM analysis on the obtained data was carried out using the following procedure: 1) We set the number of states (N) and divided the data into N groups by the K-means clustering method in which initial values were given by the K means++ method ; 2) We calculated the initial parameters of the observation probability for each group; 3) We used the VB-E step to optimize $q(Z)$ by equations (22~24) with the forward-backward algorithm; 4) We used the VB-M step to update the parameters by equations (27~29); 5) We calculated the lower bound, L_q, by using equation (30) and judging its convergence, except for the first L_q, by determining whether the difference from the previous L_q was less than 0.001%; 6) If L_q was not converged, we repeated the next iteration step by repeating steps 3) to 5); and 7) We optimized the state sequence by choosing a state with the highest probability at every frame. For the calculation in 4), we assigned $u_{i\pi} = u^A_{ij} = 1$, and different fixed values for a_D, b_D that gave maximum lower bounds for the observed trajectory data.

Heterologous expression and membrane preparation for in vitro biochemical assay

Heterologous expression of mGluR3 in HEK293 cells for *in vitro* biochemical assay was performed according to previously reported methods (*19*). The plasmid DNA (10 μg/100-mm dish) of mGluR3 or pCAG vector (mock) was transfected into HEK293

cells growing to ~40% confluency in DMEM/F12 supplemented with 10% FBS by the calcium-phosphate method. The cells were collected 48 h after transfection by centrifugation, and the pellet was washed with PBS (1 mL, pH 7.4). The cell pellet in a 1.5 mL tube was homogenized with a pellet mixer in 50% sucrose in buffer A (50 mM HEPES (pH 6.5) and 140 mM NaCl) prior to centrifugation. The supernatant containing the plasma membrane was diluted in two volumes of buffer A and recentrifuged. The membrane pellet was washed with buffer A and stored at –80 °C.

Western blotting

The mGluR3 containing membrane pellet was suspended in the sample buffer (62.5 mM Tris-HCl (pH 6.8), 4% SDS, 10% glycerol) with or without 2.5% β-mercaptoethanol (ME). After 5.5% SDS-PAGE, the electrophoresed proteins were transferred onto a polyvinylidene difluoride membrane and probed with the Rho1D4 antibody (primary antibody) and the HRP-linked anti-mouse IgG (secondary antibody, Cell Signaling #7076). Immunoreactive proteins were detected using the Amersham ECL prime Western blotting detection reagent (GE) with ImageQuant LAS 500 (GE).

[^{3}H]-Ligand-binding assay of mGluR3

The cell membranes containing mGluR3 were resuspended in HBSS (with 15 mM HEPES (pH 7.1), without $NaHCO_3$ (Sigma)), which are the same buffer conditions as for the single-molecule imaging. [^{3}H]-LY341495 binding to membranes was measured at room temperature. The membranes (1/32 of pellets from cells confluent in a 100-mm dish) were incubated with 0–1 μM [^{3}H]-LY341495 in HBSS for 30 min (final assay volume: 20 μL). After incubation, bound and free radioligands were separated by filtration through a nitrocellulose membrane (0.45 μm HATF, Millipore) using a dot-blotter (FLE396AA, ADVANTEC). The nitrocellulose membrane was washed twice with HBSS (200 μL) and dried for 1 h. The pieces of the nitrocellulose membrane were put in a scintillation cocktail (Ultima Gold, PerkinElmer), and the bound [^{3}H]-LY341495 was quantified by a liquid scintillation counter (LS6500, Beckman Coulter). Non-specific binding was measured with the mock-transfected HEK293 cell membrane. The K_d was calculated by equation 3, where EC_{50} was replaced by K_d. Displacement by LY379268 of [^{3}H]-LY341495 bound to the cell membranes expressing mGluR3 was also measured at room temperature with or without NMI137. A mixture of membranes, 100 nM [^{3}H]-LY341495, 0–100 μM LY341495, and 0 or 1 μM MNI137 in HBSS was incubated for 30 min (final assay volume: 20 μL). [^{3}H]-LY341495 was quantified as

described above. The specific binding was defined using 100 μM LY341495 as the displacer. The IC_{50} values were calculated by equation 4.

[^{35}S]-GTPγS binding assay of mGluR3

The G protein activation efficiencies of mGluR3 were measured under various ligand conditions according to a modified version of our previous method (*42*). The mGluR3-expressing membrane pellet (final concentration, 11 nM) after sucrose flotation was suspended in 0.02% n-dodecyl-*β*-D-maltopyranoside (DM; Dojindo) in buffer B (50 mM HEPES (pH 6.5), 140 mM NaCl, and 3 mM $MgCl_2$) and preincubated with ligands and G_o protein (final concentration 200 nM) purified from pig cerebral cortex. After pre-incubation for 30 min at 20 °C, the GDP/GTPγS exchange reaction was started by adding [^{35}S]-GTPγS solution. The assay mixture (20 μL) consisted of 50 mM HEPES (pH 6.5), 140 mM NaCl, 5 mM $MgCl_2$, 0.01% DM, 0.03% sodium cholate, 5 nM [^{35}S]-GTPγS, 500 nM GTPγS (cold), and 500 nM GDP. After incubation for 30 s, the reaction was terminated by adding stop solution (200 μL, 20 mM Tris/Cl (pH 7.4), 100 mM NaCl, 25 mM $MgCl_2$, 500 nM GTPγS (cold), and 500 nM GDP) and immediately filtering the sample through a nitrocellulose membrane (0.45 μm HATF, Millipore) to trap [^{35}S]-GTPγS bound to G proteins. The nitrocellulose membrane was washed three times with buffer C (200 μL, 20 mM Tris/Cl (pH 7.4), 100 mM NaCl, and 25 mM $MgCl_2$) and dried for 1 h. The pieces of the nitrocellulose membrane were put in scintillation cocktail (Ultima Gold, PerkinElmer), and the bound [^{35}S]-GTPγS was quantified by a liquid scintillation counter (LS6500, Beckman Coulter). Non-specific binding was measured using the mock-transfected HEK293 cell membrane. The EC_{50} and IC_{50} values were calculated with equations 3 and 4, respectively.

Saturation binding assay of HaloTag TMR ligands

The HEK293 cells growing to ~90% confluence on a 100-mm dish were detached using the same protocol for passage, and suspended in DMEM/F12 (4 mL) with 10% FBS. After 15 min incubation at room temperature, the transfection mixture (plasmid DNA of HaloTag-fusion mGluR3 or pcDNA3.1 vector [2 μg], P3000 reagent [4 μL], Lipofectamine 3000 reagent [5 μL], and Opti-MEM [240 μL, Gibco]) was added to the cell suspension (0.5 mL). After 2 min incubation at room temperature, the lipofectamine-treated cells were diluted with DMEM/F12 (6 mL) with 10% FBS. The cell suspension (100 μL) was added to each well of a black, collagen I-coated 96-well plate (Nunc, Thermo Fisher Scientific). After overnight incubation at 37 °C under 5% CO_2, the medium in each well was changed to 0–1 μM HaloTag TMR or SF650 ligand

solution in DMEM/F12 without phenol red (50 μL). After 15 min incubation at 37 °C under 5% CO_2, the cells were washed three times with DMEM/F12 without phenol red (100 μL), and the medium was finally replaced with 0.001% BSA/HBSS (100 μL) before quantification. Saturation binding of the HaloTag ligand was detected by a microplate reader (FlexStation 3, Molecular Devices) with the following parameters: mode, fluorescence; excitation/cut-off/emission, 530/570/580 nm for TMR, 640/665/675 nm for SF650; photomultiplier gain, automatic; flashes per read, 6; read from bottom. The background fluorescence intensity was estimated from the intensity of wells without HaloTag ligand treatment. The non-specific binding was determined by the fluorescence intensity of mock-transfected wells. The specific binding was calculated as the difference between the total binding to cells expressing HaloTag-fusion mGluR3 and the non-specific binding. The data were fitted with the Hill equation

$$\mathrm{f(x)} = \mathrm{bottom} + \frac{\mathrm{top} - \mathrm{bottom}}{(1 + \frac{EC_{50}}{x})^n} \quad (31)$$

where n is the Hill coefficient.

Supplementary Materials

Fig. S1. Evaluation of the effect of HaloTag fusion to mGluR3

Fig. S2. Saturation binding assay of TMR ligands to mGluR3 with HaloTag

Fig. S3. Example of the VB-HMM analysis of mGluR3 trajectories

Fig. S4. Dose-dependent change in the time constants of the state transition

Fig. S5. Dose-dependent change in the diffusion coefficient of each diffusion state

Fig. S6. Correlation between mean oligomer size and receptor density in various ligand conditions

Fig. S7. Correlation between D_{Av} and receptor density in various ligand conditions

Fig. S8. MSD-Δt plots of the trajectories of GPCRs with or without agonist

Movie 1. TIRFM of TMR-labeled mGluR3 molecules on a HEK293 cell

Movie 2. Accumulation of mGluR3 molecules followed by disappearance with rapid movement

Movie 3. Dual-color TIRFM of TMR-labeled mGluR3 and GFP-labeled CLC

Movie 4. TIRFM of various GPCR molecules on a HEK293 cell with and without agonist

References:

1. R. Fredriksson, M. C. Lagerstrom, L. G. Lundin, H. B. Schioth, The G-protein-coupled receptors in the human genome form five main families. Phylogenetic analysis, paralogon groups, and fingerprints. *Mol Pharmacol* **63**, 1256-1272 (2003); published online EpubJun (10.1124/mol.63.6.1256).
2. C. Munk, V. Isberg, S. Mordalski, K. Harpsoe, K. Rataj, A. S. Hauser, P. Kolb, A. J. Bojarski, G. Vriend, D. E. Gloriam, GPCRdb: the G protein-coupled receptor database - an introduction. *Br J Pharmacol* **173**, 2195-2207 (2016); published online EpubJul (10.1111/bph.13509).
3. R. Santos, O. Ursu, A. Gaulton, A. P. Bento, R. S. Donadi, C. G. Bologa, A. Karlsson, B. Al-Lazikani, A. Hersey, T. I. Oprea, J. P. Overington, A comprehensive map of molecular drug targets. *Nat Rev Drug Discov* **16**, 19-34 (2017); published online EpubJan (10.1038/nrd.2016.230).
4. X. L. Tang, Y. Wang, D. L. Li, J. Luo, M. Y. Liu, Orphan G protein-coupled receptors (GPCRs): biological functions and potential drug targets. *Acta Pharmacol Sin* **33**, 363-371 (2012); published online EpubMar (10.1038/aps.2011.210).
5. R. Zhang, X. Xie, Tools for GPCR drug discovery. *Acta Pharmacol Sin* **33**, 372-384 (2012); published online EpubMar (10.1038/aps.2011.173).
6. Y. Sako, S. Minoguchi, T. Yanagida, Single-molecule imaging of EGFR signalling on the surface of living cells. *Nat Cell Biol* **2**, 168-172 (2000); published online EpubMar (10.1038/35004044).
7. Y. Miyanaga, S. Matsuoka, M. Ueda, Single-molecule imaging techniques to visualize chemotactic signaling events on the membrane of living Dictyostelium cells. *Methods Mol Biol* **571**, 417-435 (2009)10.1007/978-1-60761-198-1_28).
8. M. Hiroshima, Y. Saeki, M. Okada-Hatakeyama, Y. Sako, Dynamically varying interactions between heregulin and ErbB proteins detected by single-molecule analysis in living cells. *Proc Natl Acad Sci U S A* **109**, 13984-13989 (2012); published online EpubAug 28

(10.1073/pnas.1200464109).

9. J. A. Hern, A. H. Baig, G. I. Mashanov, B. Birdsall, J. E. Corrie, S. Lazareno, J. E. Molloy, N. J. Birdsall, Formation and dissociation of M1 muscarinic receptor dimers seen by total internal reflection fluorescence imaging of single molecules. *Proc Natl Acad Sci U S A* **107**, 2693-2698 (2010); published online EpubFeb 9 (10.1073/pnas.0907915107).

10. R. S. Kasai, K. G. Suzuki, E. R. Prossnitz, I. Koyama-Honda, C. Nakada, T. K. Fujiwara, A. Kusumi, Full characterization of GPCR monomer-dimer dynamic equilibrium by single molecule imaging. *J Cell Biol* **192**, 463-480 (2011); published online EpubFeb 7 (10.1083/jcb.201009128).

11. D. Calebiro, F. Rieken, J. Wagner, T. Sungkaworn, U. Zabel, A. Borzi, E. Cocucci, A. Zurn, M. J. Lohse, Single-molecule analysis of fluorescently labeled G-protein-coupled receptors reveals complexes with distinct dynamics and organization. *Proc Natl Acad Sci U S A* **110**, 743-748 (2013); published online EpubJan 8 (10.1073/pnas.1205798110).

12. A. Tabor, S. Weisenburger, A. Banerjee, N. Purkayastha, J. M. Kaindl, H. Hubner, L. Wei, T. W. Gromer, J. Kornhuber, N. Tschammer, N. J. Birdsall, G. I. Mashanov, V. Sandoghdar, P. Gmeiner, Visualization and ligand-induced modulation of dopamine receptor dimerization at the single molecule level. *Sci Rep* **6**, 33233 (2016); published online EpubSep 12 (10.1038/srep33233).

13. N. Kunishima, Y. Shimada, Y. Tsuji, T. Sato, M. Yamamoto, T. Kumasaka, S. Nakanishi, H. Jingami, K. Morikawa, Structural basis of glutamate recognition by a dimeric metabotropic glutamate receptor. *Nature* **407**, 971-977 (2000); published online EpubOct 26 (

14. R. Vafabakhsh, J. Levitz, E. Y. Isacoff, Conformational dynamics of a class C G-protein-coupled receptor. *Nature* **524**, 497-501 (2015); published online EpubAug 27 (10.1038/nature14679).

15. M. Tateyama, H. Abe, H. Nakata, O. Saito, Y. Kubo, Ligand-induced rearrangement of the dimeric metabotropic glutamate receptor 1alpha. *Nat Struct Mol Biol* **11**, 637-642 (2004); published online EpubJul (

16. M. Yanagawa, T. Yamashita, Y. Shichida, Comparative fluorescence resonance energy transfer analysis of metabotropic glutamate receptors: implications about the dimeric arrangement and rearrangement upon ligand bindings. *J Biol Chem* **286**, 22971-22981 (2011); published online EpubJul 1 (10.1074/jbc.M110.206870).

17. L. Xue, X. Rovira, P. Scholler, H. Zhao, J. Liu, J. P. Pin, P. Rondard, Major ligand-induced rearrangement of the heptahelical domain interface in a GPCR dimer. *Nat Chem Biol* **11**, 134-140 (2015); published online EpubFeb (10.1038/nchembio.1711).

18. C. Brock, N. Oueslati, S. Soler, L. Boudier, P. Rondard, J. P. Pin, Activation of a dimeric metabotropic glutamate receptor by intersubunit rearrangement. *J Biol Chem* **282**, 33000-33008

(2007); published online EpubNov 9 (10.1074/jbc.M702542200).

19. M. Yanagawa, T. Yamashita, Y. Shichida, Glutamate acts as a partial inverse agonist to metabotropic glutamate receptor with a single amino acid mutation in the transmembrane domain. *J Biol Chem* **288**, 9593-9601 (2013); published online EpubApr 5 (10.1074/jbc.M112.437780).

20. B. K. Atwood, J. Lopez, J. Wager-Miller, K. Mackie, A. Straiker, Expression of G protein-coupled receptors and related proteins in HEK293, AtT20, BV2, and N18 cell lines as revealed by microarray analysis. *BMC Genomics* **12**, 14 (2011)10.1186/1471-2164-12-14).

21. K. Hemstapat, H. Da Costa, Y. Nong, A. E. Brady, Q. Luo, C. M. Niswender, G. D. Tamagnan, P. J. Conn, A novel family of potent negative allosteric modulators of group II metabotropic glutamate receptors. *J Pharmacol Exp Ther* **322**, 254-264 (2007); published online EpubJul (10.1124/jpet.106.117093).

22. A. S. Tora, X. Rovira, I. Dione, H. O. Bertrand, I. Brabet, Y. De Koninck, N. Doyon, J. P. Pin, F. Acher, C. Goudet, Allosteric modulation of metabotropic glutamate receptors by chloride ions. *FASEB J* **29**, 4174-4188 (2015); published online EpubOct (10.1096/fj.14-269746).

23. J. O. DiRaddo, E. J. Miller, C. Bowman-Dalley, B. Wroblewska, M. Javidnia, E. Grajkowska, B. B. Wolfe, D. C. Liotta, J. T. Wroblewski, Chloride is an Agonist of Group II and III Metabotropic Glutamate Receptors. *Mol Pharmacol* **88**, 450-459 (2015); published online EpubSep (10.1124/mol.114.096420).

24. R. R. Neubig, M. Spedding, T. Kenakin, A. Christopoulos, N. International Union of Pharmacology Committee on Receptor, C. Drug, International Union of Pharmacology Committee on Receptor Nomenclature and Drug Classification. XXXVIII. Update on terms and symbols in quantitative pharmacology. *Pharmacol Rev* **55**, 597-606 (2003); published online EpubDec (10.1124/pr.55.4.4).

25. F. Persson, M. Linden, C. Unoson, J. Elf, Extracting intracellular diffusive states and transition rates from single-molecule tracking data. *Nat Methods* **10**, 265-269 (2013); published online EpubMar (10.1038/nmeth.2367).

26. K. Okamoto, Y. Sako, Variational Bayes analysis of a photon-based hidden Markov model for single-molecule FRET trajectories. *Biophys J* **103**, 1315-1324 (2012); published online EpubSep 19 (10.1016/j.bpj.2012.07.047).

27. A. Kusumi, Y. Sako, M. Yamamoto, Confined lateral diffusion of membrane receptors as studied by single particle tracking (nanovid microscopy). Effects of calcium-induced differentiation in cultured epithelial cells. *Biophys J* **65**, 2021-2040 (1993); published online EpubNov (10.1016/S0006-3495(93)81253-0).

28. A. Kusumi, T. A. Tsunoyama, K. M. Hirosawa, R. S. Kasai, T. K. Fujiwara, Tracking single molecules at work in living cells. *Nat Chem Biol* **10**, 524-532 (2014); published online EpubJul

(10.1038/nchembio.1558).

29. S. Mangmool, H. Kurose, G(i/o) protein-dependent and -independent actions of Pertussis Toxin (PTX). *Toxins (Basel)* **3**, 884-899 (2011); published online EpubJul (10.3390/toxins3070884).

30. M. Nobles, A. Benians, A. Tinker, Heterotrimeric G proteins precouple with G protein-coupled receptors in living cells. *Proc Natl Acad Sci U S A* **102**, 18706-18711 (2005); published online EpubDec 20 (10.1073/pnas.0504778102).

31. C. Gales, J. J. Van Durm, S. Schaak, S. Pontier, Y. Percherancier, M. Audet, H. Paris, M. Bouvier, Probing the activation-promoted structural rearrangements in preassembled receptor-G protein complexes. *Nat Struct Mol Biol* **13**, 778-786 (2006); published online EpubSep (10.1038/nsmb1134).

32. K. Qin, C. Dong, G. Wu, N. A. Lambert, Inactive-state preassembly of G(q)-coupled receptors and G(q) heterotrimers. *Nat Chem Biol* **7**, 740-747 (2011); published online EpubOct (10.1038/nchembio.642).

33. M. Arizono, H. Bannai, K. Nakamura, F. Niwa, M. Enomoto, T. Matsu-Ura, A. Miyamoto, M. W. Sherwood, T. Nakamura, K. Mikoshiba, Receptor-selective diffusion barrier enhances sensitivity of astrocytic processes to metabotropic glutamate receptor stimulation. *Sci Signal* **5**, ra27 (2012); published online EpubApr 3 (10.1126/scisignal.2002498).

34. M. T. Drake, S. K. Shenoy, R. J. Lefkowitz, Trafficking of G protein-coupled receptors. *Circ Res* **99**, 570-582 (2006); published online EpubSep 15 (10.1161/01.RES.0000242563.47507.ce).

35. M. A. Puthenveedu, M. von Zastrow, Cargo regulates clathrin-coated pit dynamics. *Cell* **127**, 113-124 (2006); published online EpubOct 6 (10.1016/j.cell.2006.08.035).

36. A. G. Henry, J. N. Hislop, J. Grove, K. Thorn, M. Marsh, M. von Zastrow, Regulation of endocytic clathrin dynamics by cargo ubiquitination. *Dev Cell* **23**, 519-532 (2012); published online EpubSep 11 (10.1016/j.devcel.2012.08.003).

37. I. Gaidarov, F. Santini, R. A. Warren, J. H. Keen, Spatial control of coated-pit dynamics in living cells. *Nat Cell Biol* **1**, 1-7 (1999); published online EpubMay (10.1038/8971).

38. K. A. K. Tanaka, K. G. N. Suzuki, Y. M. Shirai, S. T. Shibutani, M. S. H. Miyahara, H. Tsuboi, M. Yahara, A. Yoshimura, S. Mayor, T. K. Fujiwara, A. Kusumi, Membrane molecules mobile even after chemical fixation. *Nature Methods* **7**, 865-866 (2010); published online EpubNov (10.1038/nmeth.f.314).

39. Z. Xiao, X. Ma, Y. Jiang, Z. Zhao, B. Lai, J. Liao, J. Yue, X. Fang, Single-molecule study of lateral mobility of epidermal growth factor receptor 2/HER2 on activation. *J Phys Chem B* **112**, 4140-4145 (2008); published online EpubApr 3 (10.1021/jp710302j).

40. K. M. Wilson, I. E. Morrison, P. R. Smith, N. Fernandez, R. J. Cherry, Single particle tracking of cell-surface HLA-DR molecules using R-phycoerythrin labeled monoclonal antibodies and fluorescence digital imaging. *J Cell Sci* **109 (Pt 8)**, 2101-2109 (1996); published online

EpubAug (

41. M. Beal, (2003).

42. M. Yanagawa, T. Yamashita, Y. Shichida, Activation Switch in the Transmembrane Domain of Metabotropic Glutamate Receptor. *Molecular Pharmacology* **76**, 201-207 (2009); published online EpubJul (10.1124/mol.109.056549).

Acknowledgments: We would like to thank J. Nathans for providing us with the HEK293S cell line, R. S. Molday for the Rho 1D4-producing hybridoma. We would also like to thank T. Yanagida for critical reading of the manuscript. **Funding**: This work was supported by the Ministry of Education, Culture, Sports, Science and Technology (MEXT), Japan [Grants-in-Aid for Scientific Research 26840055 and 16K18533] and RIKEN special postdoctoral researcher (SPDR) fellowship for M.Y.
Author contributions: M.Y. designed and performed most of the experiments reported. Y. Sako provided guidance throughout. M.H. developed the program of VB-HMM analysis. Y.T. and M.U. upgraded the program of SMT analysis. M.Y., T.Y., and Y.Shichida constructed cDNAs of mGluR3, and purified G_o protein and Rho1D4 antibody. M.M. constructed cDNA of GFP-tagged CLC. M.Y. and Y. Sako wrote the manuscript. M.H., M.U., Y.T., T.Y., and Y. Shichida advised on experiments and manuscript preparation. **Competing interests**: The authors declare no conflict of interest. The results presented in the paper has been filed (patent number 2017-084803) in Japan.

Figures:

Figure 1

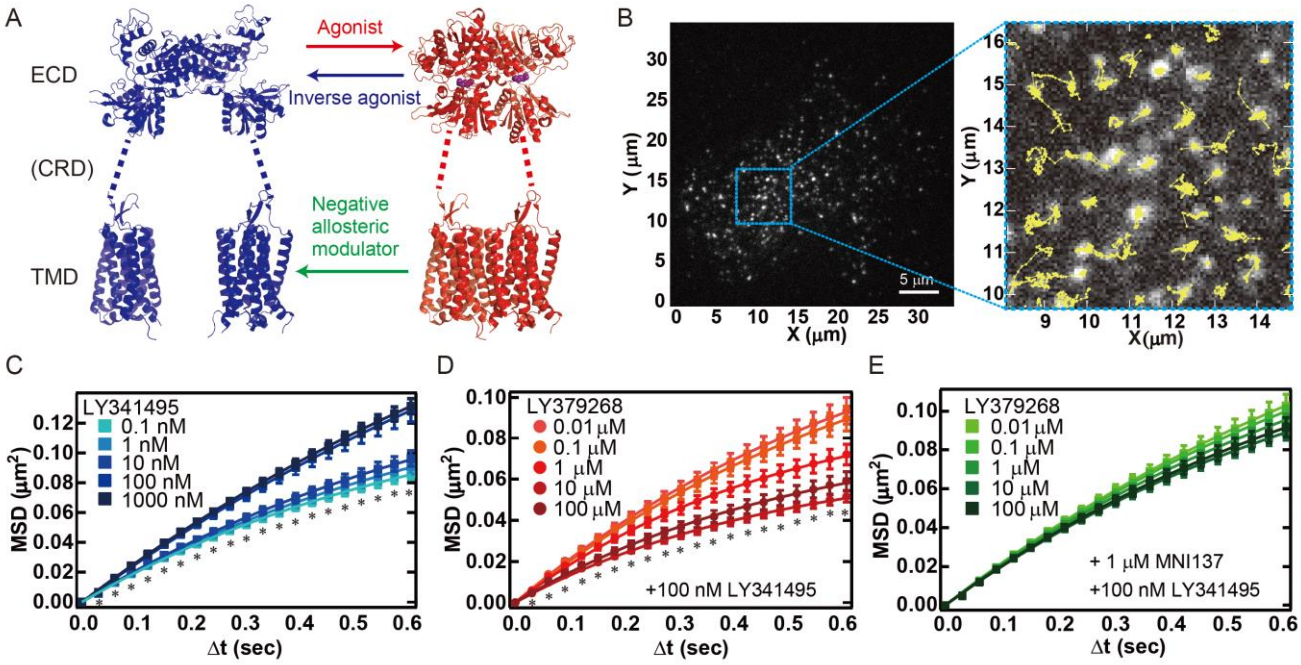

Fig. 1. **Activation model, TIRFM image, MSD-Δt plots of mGluR**

(A) Activation model of mGluR. The crystal structures of ECDs of mGluR1 in the inactive (blue: 1EWT) and active states (red: 1EWK) are constructed with PyMol (http://www.pymol.org/). The crystal structure of the TMD (blue and red: 4OR2) is also shown.

(B) Example TIRFM image of HEK293 cell expressing TMR-labeled mGluR3 (left panel: whole image, right panel: enlarged view of the blue dashed square in the left panel). The trajectories of mGluR3 molecules are shown as yellow lines in the right panel.

(C–E) MSD-Δ*t* plots of the trajectories of mGluR3 under various ligand conditions. Inverse agonist (LY341495) dependency is shown in (C). Agonist (LY379268) dependencies at 100 nM LY314195 without (D) and with (E) 1 μM MNI137. All the data are shown as mean ± SEM (n = 20 cells). * Significant difference in MSD among five ligand conditions at each Δ*t* ($p < 0.01$; one-way ANOVA).

Figure 2

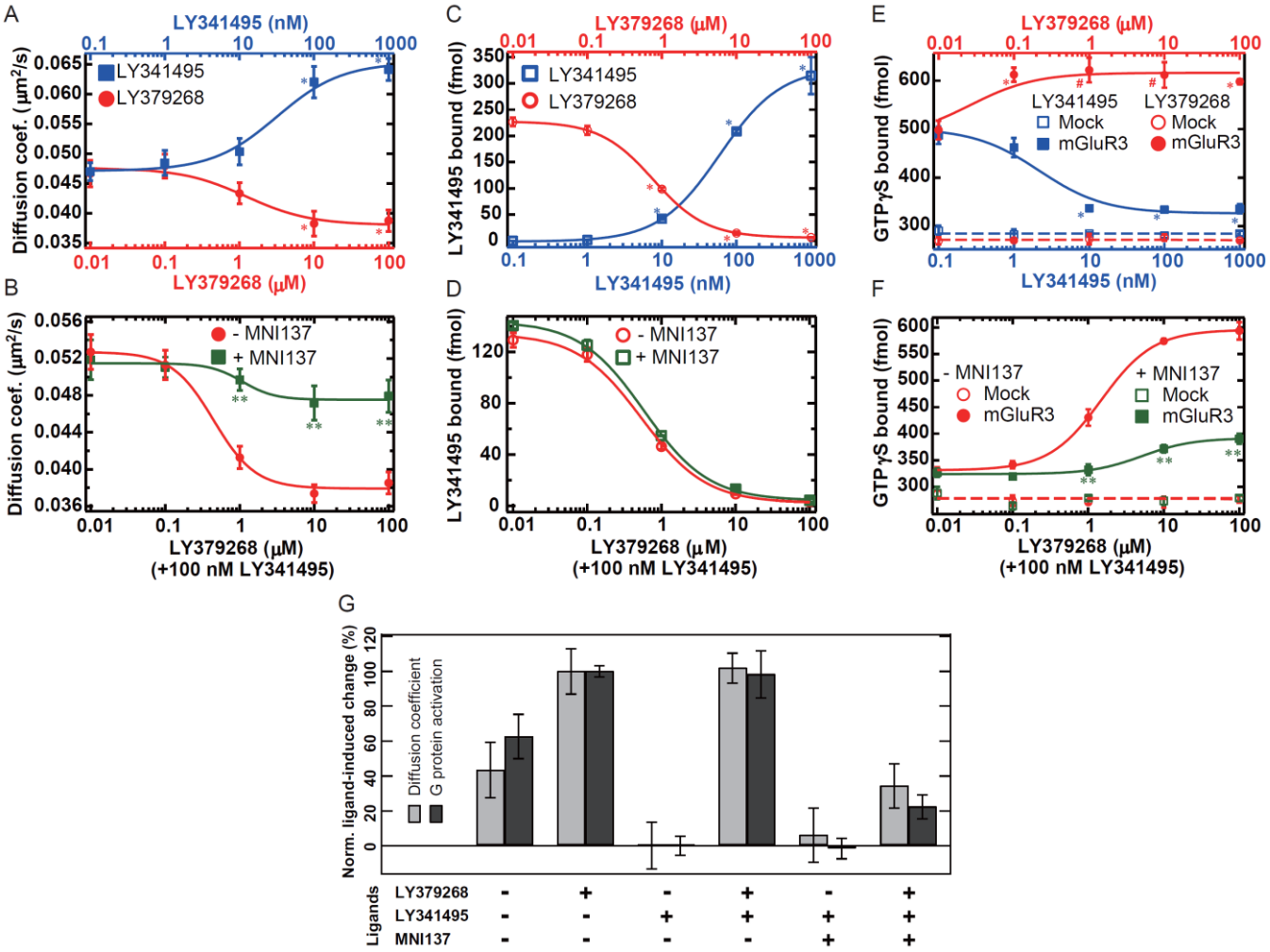

Fig. 2. Comparison of diffusion, ligand occupancy, and G protein activation of mGluR3

(A, B) Dose-dependent changes of D_{Av}. LY341495- (blue squares, EC_{50}: 28.2 ± 0.9 nM) and LY379268- (red circles, EC_{50}: 1.19 ± 0.02 μM) dependency without other ligands are shown in (A). LY379268-dependencies at 100 nM LY341495 without (red circles, EC_{50}: 1.03 ± 0.08 μM) and with (green squares, EC_{50}: 0.34 ± 0.003 μM) 1 μM MNI137 are shown in (B). All the data are shown as mean ± SEM (n = 20 cells). * Significant difference compared with the leftmost point in each curve in (A) (p < 0.01; t-test, two-tailed). ** Significant difference with and without 1 μM MNI137 in (B) (p < 0.01; t-test, two-tailed).

(C, D) Dose-dependent changes of [^{3}H]-LY341495 binding. [^{3}H]-LY341495 saturation binding (C, blue squares, K_d: 47.4 ± 1.7 nM). Replacement of 100 nM [^{3}H]-LY341495 with LY379268 in the absence (C and D, red circles, IC_{50}: 0.55 ± 0.08 μM) and presence (D, green squares, IC_{50}: 0.60 ± 0.03 μM) of 1 μM MNI137. All the data are shown as mean ± SEM (n = 3 independent experiments). The same mGluR3-transfected cell membrane preparation was analyzed within the same panel. * Significant difference compared with the leftmost point in each curve in (C) ($p < 0.01$; t-test, two-tailed). No significant difference was detected with and without 1 μM MNI137 in (D) ($p > 0.05$; t-test, two-tailed).

(E, F) Dose-dependent changes in G protein activation efficiency of mGluR3-transfected cell membrane. LY341495- (blue closed squares, IC_{50}: 2.11 ± 0.18 nM) and LY379268- (red closed circles, EC_{50}: 0.025 ± 0.0029 μM) dependencies without other ligands are shown in (E). LY379268-dependencies at 100 nM LY341495 without (red closed circles, EC_{50}: 1.77 ± 0.39 μM) and with (green closed squares, EC_{50}: 9.34 ± 4.44 μM) 1 μM MNI137 are shown in (F). Open circles and squares indicate G protein activation efficiency of mock-transfected cell membrane under the same ligand conditions as for closed circles and squares, respectively. All the data are shown as mean ± SEM (n = 3–5 independent experiments). *, # Significant differences compared with the leftmost point in each curve in (E) ($p < 0.01$ and $p < 0.03$, respectively; t-test, two-tailed). ** Significant difference with and without 1 μM MNI137 in (F) ($p < 0.01$; t-test, two-tailed).

(G) Comparison of ligand-induced changes of D_{Av} and G protein activation efficiency in the absence (–) or presence (+) of the ligands (100 μM LY379268, 100 nM LY341495, 1 μM MNI137). Data in the presence of 100 nM LY341495 without other ligands are normalized as 0%, and data in the presence of 100 μM LY379268 without other ligands are normalized as 100%. All the data are shown as mean ± SEM (D_{Av}: n = 20 cells, G protein activation efficiency: n = 3–5 independent experiments).

Figure 3

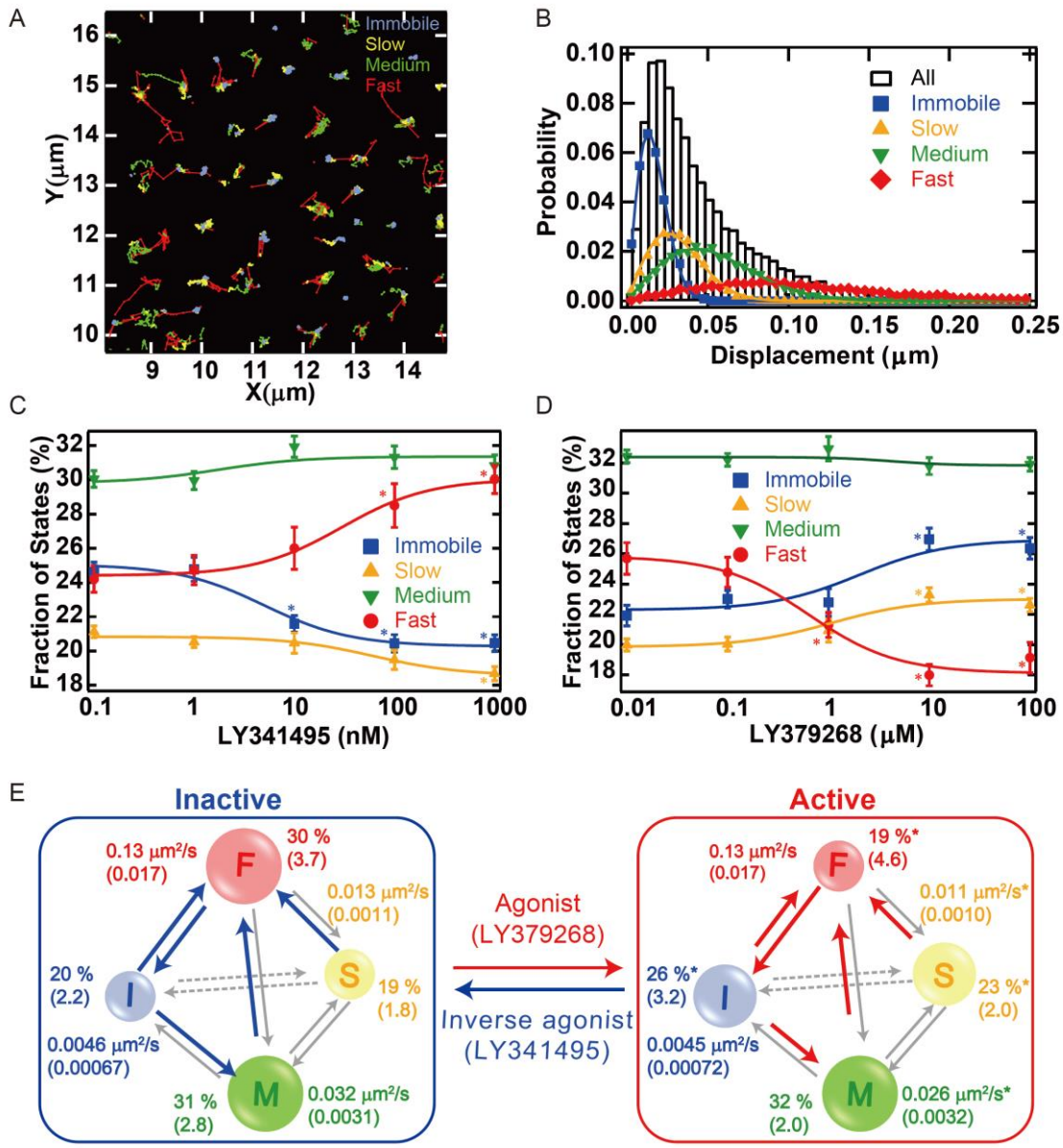

Fig. 3. VB-HMM analysis of the trajectories of mGluR3 molecules

(A) Every step in the trajectories in Fig. 1B was categorized into four diffusion states. The immobile, slow, medium, and fast states are shown in blue, yellow, green, and red, respectively.

(B) Histogram of the displacement during 30.5 ms of all the trajectories (open black bars; 28,092 steps from 573 trajectories) on a cell divided into four single-step distributions of random walks (equation 6, Methods). The immobile, slow, medium, and fast states are shown in blue, yellow, green, and red, respectively.

(C, D) Dose-dependent changes of fractions of the diffusion states. LY341495 dependency is shown in (C). LY379268 dependencies under 100 nM LY314195 are shown in (D). The immobile, slow, medium, and fast states are shown in blue, yellow, green, and red, respectively. All the data are shown as mean ± SEM (n = 20 cells). * Significant difference in the fractions compared with the leftmost point in each curve ($p < 0.01$; t-test, two-tailed).

(E) Four state transition diagrams of mGluR3 under inactive (1 μM LY314195) and active (100 μM LY379268 with 100 nM LY341495) ligand conditions. The diffusion coefficient and fraction of each state are shown next to the circles, the size of which reflects the size of the fraction. The SEM is indicated in parentheses (n = 20 cells). The arrows between states reflect the rate constants of the state transition estimated from Fig. S4. The significant changes in rate constants between the two conditions in Fig. S4 are shown as colored arrows (inactive: blue, active: red). * Significant difference in the fractions or in the diffusion coefficients compared with the inactive ligand conditions ($p < 0.01$; t-test, two-tailed).

Figure 4

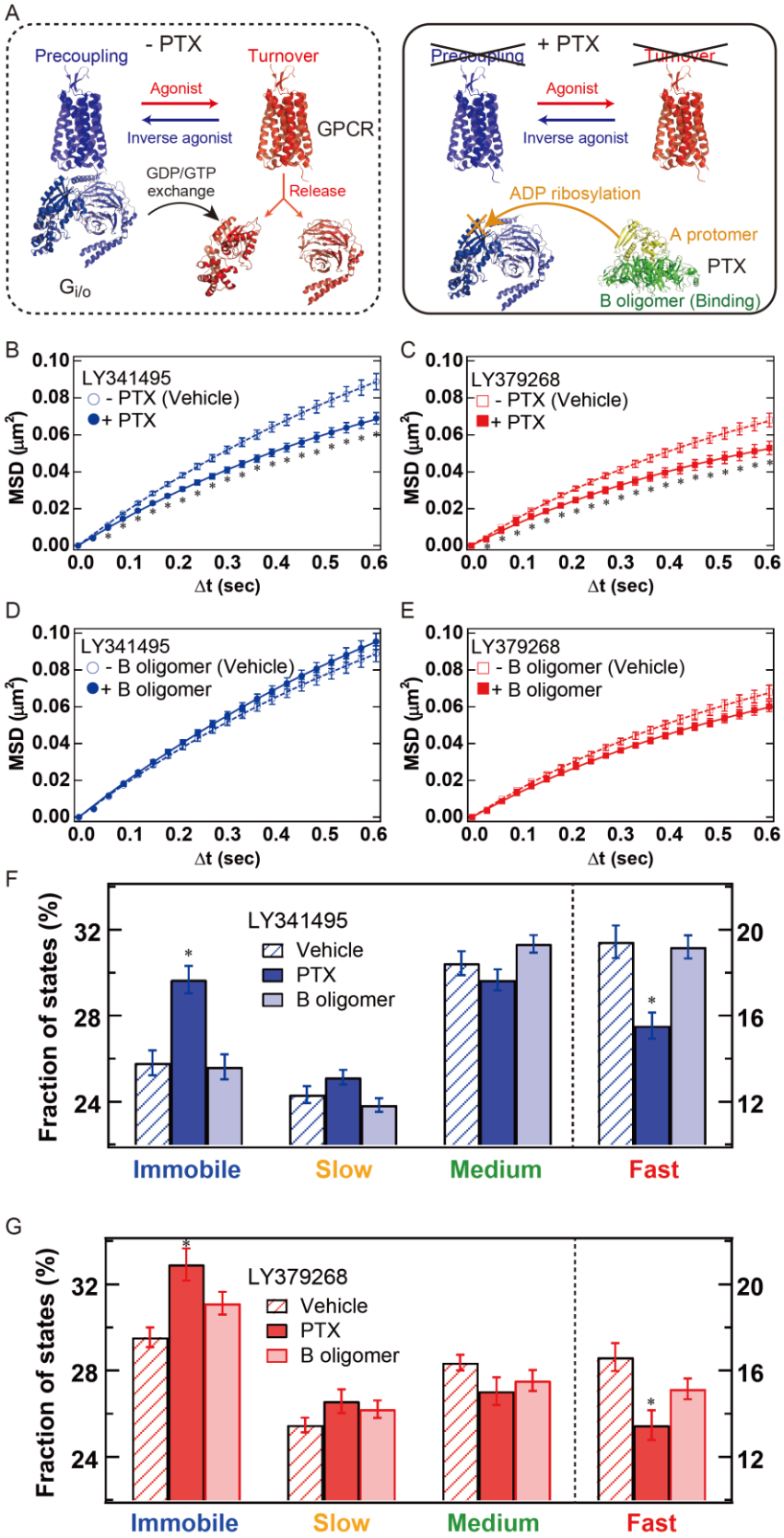
A
- PTX
Precoupling
Turnover
Agonist
Inverse agonist
GPCR
GDP/GTP exchange
Release
Gi/o
+ PTX
Precoupling
Turnover
Agonist
Inverse agonist
ADP ribosylation
A protomer
PTX
B oligomer (Binding)
B
LY341495
- PTX (Vehicle)
+ PTX
MSD (μm²)
Δt (sec)
C
LY379268
- PTX (Vehicle)
+ PTX
MSD (μm²)
Δt (sec)
D
LY341495
- B oligomer (Vehicle)
+ B oligomer
MSD (μm²)
Δt (sec)
E
LY379268
- B oligomer (Vehicle)
+ B oligomer
MSD (μm²)
Δt (sec)
F
LY341495
Vehicle
PTX
B oligomer
Fraction of states (%)
Immobile
Slow
Medium
Fast
G
LY379268
Vehicle
PTX
B oligomer
Fraction of states (%)
Immobile
Slow
Medium
Fast

Fig. 4. Effects of the PTX treatment on the molecular behavior of mGluR3

(A) Schematic model of the effect of PTX on the GPCR/$G_{i/o}$ protein interaction. Without PTX treatment (left panel), a certain amount of GPCR is precoupled with $G_{i/o}$ protein in the inactive state [28-30]. The $G_{i/o}$ protein is released from GPCR upon activation after the GDP/GTP exchange reaction. GPCR in the active state continuously turns over the G proteins, during which the transient binding and release of $G_{i/o}$ protein occur repeatedly. In contrast, the precoupling and turnover of $G_{i/o}$ protein are inhibited by ADP ribosylation after PTX treatment (right panel). The crystal structures (4OR2, 1GP2, 1GIA, and 1PRT) are drawn with PyMol as representative of GPCR, trimeric G protein, activated Gα, and PTX, respectively.

(B-E) Comparison of MSD-Δt plots of mGluR3 trajectories with or without PTX. The MSD-Δ*t* plots for the inactive (100 nM LY314195) and active (100 μM LY379268) ligand conditions are shown in (B) and (C), respectively. Similar comparisons of MSD-Δ*t* plots with or without the PTX B oligomer for the inactive and active ligand conditions are shown in (D) and (E), respectively. * Significant difference compared with vehicle conditions ($p < 0.01$; t-test, two-tailed).

(F, G) Comparison of fractions of the diffusion states estimated from VB-HMM analysis. Results from the same experiments in (B–G) are shown as mean ± SEM (n = 20 cells). * Significant difference compared with vehicle conditions ($p < 0.01$; t-test, two-tailed).

Figure 5

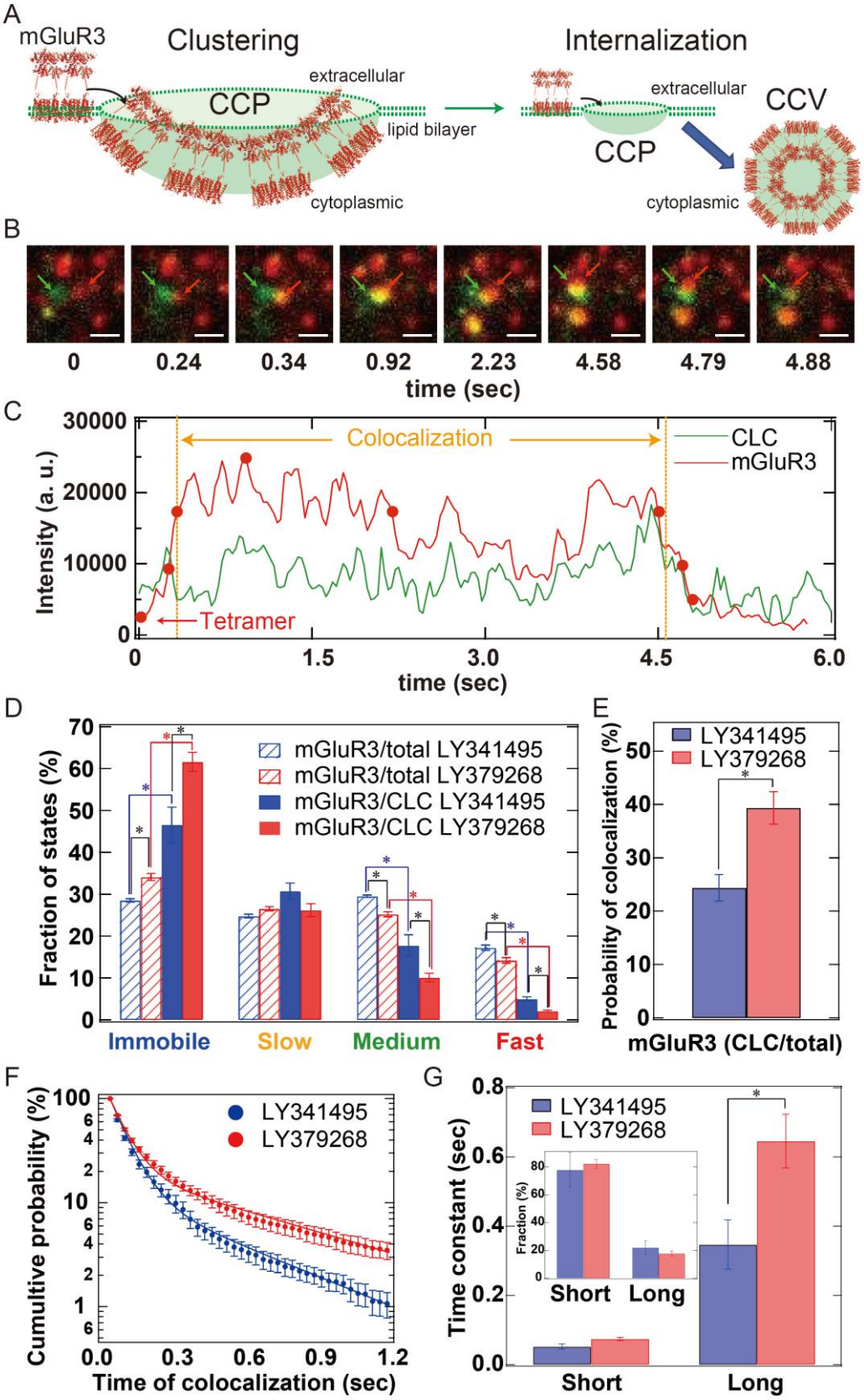
A
mGluR3
Clustering
extracellular
CCP
lipid bilayer
cytoplasmic
Internalization
extracellular
CCV
CCP
cytoplasmic
B
0
0.24
0.34
0.92
2.23
4.58
4.79
4.88
time (sec)
C
Colocalization
CLC
mGluR3
Intensity (a. u.)
Tetramer
time (sec)
D
Fraction of states (%)
mGluR3/total LY341495
mGluR3/total LY379268
mGluR3/CLC LY341495
mGluR3/CLC LY379268
Immobile
Slow
Medium
Fast
E
LY341495
LY379268
Probability of colocalization (%)
mGluR3 (CLC/total)
F
LY341495
LY379268
Cumultive probability (%)
Time of colocalization (sec)
G
LY341495
LY379268
Time constant (sec)
Fraction (%)
Short
Long
Short
Long

Fig. 5. Colocalization analysis of mGluR3 and CLC

(A) Schematic of mGluR3 clustering in a CCP followed by internalization.

(B) Representative images of colocalization of TMR-labeled mGluR3 (red) and GFP-labeled CLC (green). mGluR3 forms a cluster during the colocalization with CLC after 0.34 s and disappears after 4.5 s. Scale bars indicate 1 μm.

(C) Intensity changes of the particles in B indicated by red and green arrows. A rapid increase in the TMR-labeled mGluR3 intensity coincided with the colocalization with GFP-labeled CLC. TMR and GFP intensities decreased simultaneously after 4.5 s.

(D) Comparison of fractions of the diffusion states estimated from VB-HMM analysis. The fractions estimated from the total trajectories of mGluR3 in the inactive (100 nM LY314195) and active (100 μM LY379268) conditions are indicated by blue and red shaded bars, respectively. The fractions estimated from the mGluR3 trajectories colocalized with CLC in the inactive and active conditions are indicated by blue and red solid bars, respectively.

(E) Proportion of mGluR3 colocalized with CLC to the total trajectories in the inactive (blue) and active (red) conditions.

(F, G) Cumulative probability histograms of the duration of colocalization under the inactive (blue) and active (red) ligand conditions. Curves in c are fitted by a two-component exponential function (equation 8 in Methods) to show the time constants and fraction (inset) of colocalization in g.

All the data in Fig. 5D-G are shown as the mean ± SEM (n = 15 cells for inactive ligand conditions, 18 cells for active ligand conditions). * Significant difference ($p < 0.01$; t-test, two-tailed).

GPCR	Class	Group	Cluster	Endogenous ligand	G protein selectivity	D_{Av} ($\mu m^2/s$) Vehicle	Ligand	t-test p value	Compounds tested
ADRB2	A	α	amine	adrenaline	G_s	0.078 ± 0.0024	0.051 ± 0.0023	1.2E-09	Isoproterenol (10 μM)
HTR2A	A	α	amine	serotonine	G_q/G_i	0.079 ± 0.0022	0.065 ± 0.0034	2.1E-03	serotonine (10 μM)
HRH1	A	α	amine	histamine	G_q	0.064 ± 0.0023	0.045 ± 0.0025	1.1E-06	histamine (1 μM)
ADORA2A	A	α	MECA	adenosine	G_s	0.066 ± 0.0022	0.058 ± 0.0016	8.0E-03	NECA (10 μM)
FFAR4	A	α	melatonin	free fatty acid	G_q	0.083 ± 0.0025	0.048 ± 0.0073	3.5E-13	DHA (100 nM)
CXCR4	A	γ	chemokine	chemokine	G_i	0.087 ± 0.0034	0.068 ± 0.0017	1.7E-05	CXCL12 (20 nM)
F2R	A	δ	purin	thrombin	$G_q/G_i/G_{12}$	0.084 ± 0.0041	0.060 ± 0.0017	1.4E-05	TRAP-6 (10 μM)
GCGR	B	secretin	peptide	glucagon	G_s/G_q	0.075 ± 0.0028	0.042 ± 0.0025	8.7E-11	glucagon (1 μM)
mGluR3	C	-	amino acid	glutamate	G_i	0.047 ± 0.0022 0.047 ± 0.0015	0.039 ± 0.0018 0.064 ± 0.0018	9.1E-03 1.6E-08	LY379268 (100 μM) LY341495 (1 μM)

Table 1: Comparison of D_{Av} of nine GPCRs in various phylogenetic positions with or without ligands

The class, group, and cluster of GPCRs are listed according to previous reports[1,2]. D_{Av} was calculated from the MSD in Fig. S8 based on equations 1 and 2 in Methods. All the data are shown as mean ± SEM (n = 20 cells). The p values of the significant difference between vehicle and ligand conditions were calculated based on Welch's t-test, two-tailed. Under the ligand conditions, GPCR-expressing HEK293 cells were stimulated by the compound listed in the rightmost column.

Supplementary Materials:

Supplemental Figures:

Fig. S1

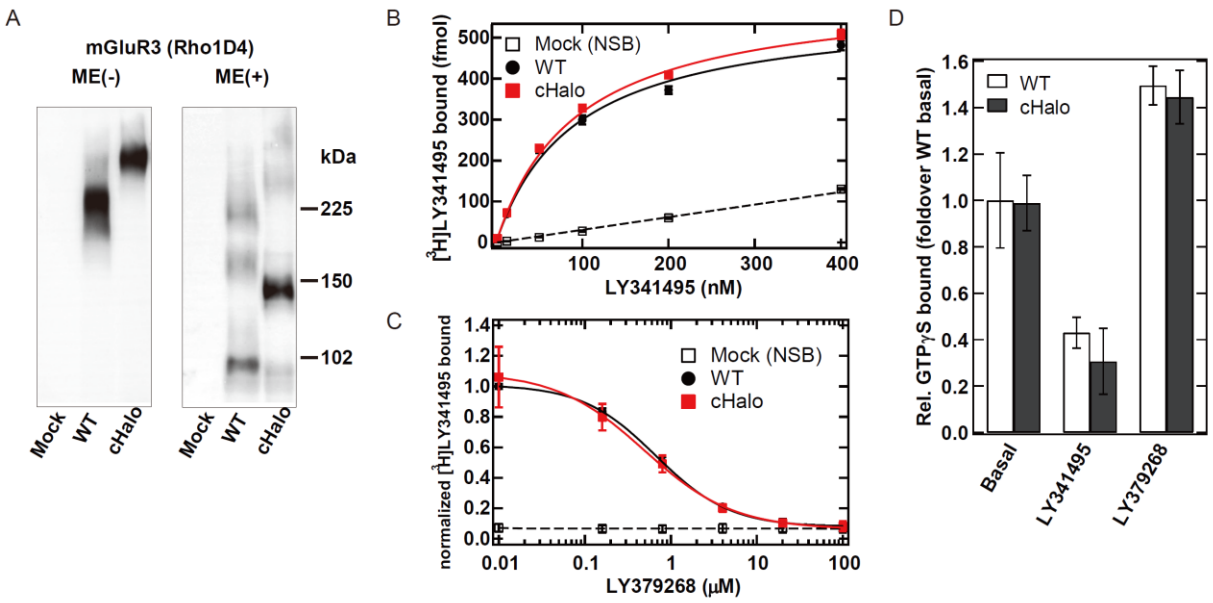

Fig. S1. Evaluation of the effect of HaloTag fusion to mGluR3

(A) Western blotting analysis of mGluR3 with and without HaloTag at the C-terminal end (cHalo and WT, respectively). Dimer bands were detected without ME in the left panel. The reduction of the disulphide bond linking the ECDs of mGluR3 by ME resulted in the appearance of monomer bands (right panel).

(B, C) Comparison of ligand binding of mGluR3 with and without HaloTag. No significant difference was observed in the saturation binding of [^{3}H]-LY341495 in (B) and in the competitive binding of [^{3}H]-LY341495 and LY379268 in (C).

(D) Comparison of G protein activation by mGluR3 with and without HaloTag. No significant difference was observed in the activities between WT and cHalo in the basal, 1 μM LY341495, and 100 μM LY379268 conditions.

All data in (B-D) are shown as mean ± SEM (n = 3 independent experiments).

Fig. S2

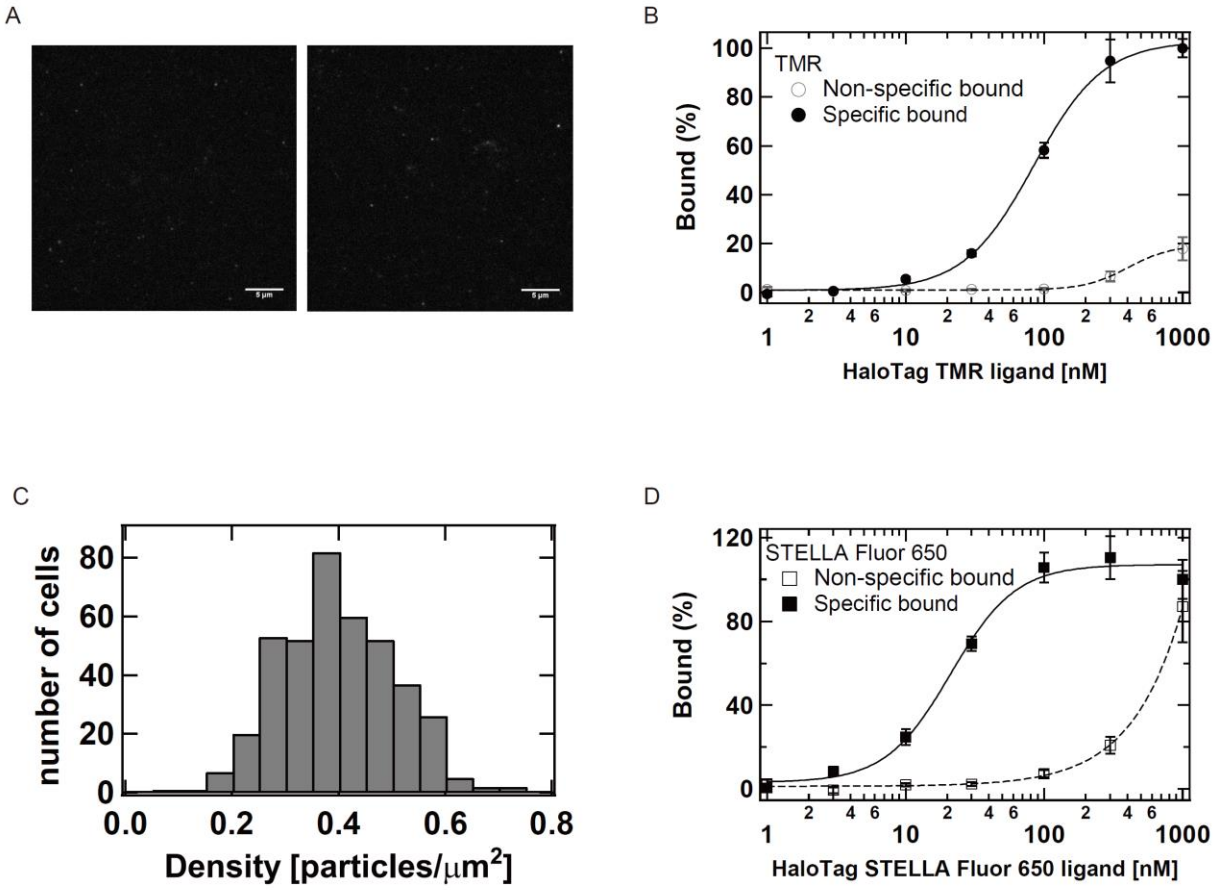

Fig. S2. Saturation binding assay of TMR ligands to mGluR3 with HaloTag
(A) TIRFM images of the non-specific binding of TMR ligands to HEK293 cells and coverslips. The experimental and image processing conditions are the same as in Fig. 1B.

(B) Specific and non-specific binding of HaloTag TMR ligands to HEK293 cells expressing HaloTag fusion mGluR3 and to mock transfected cells in 96-well plates. Data are shown as mean ± SEM (n = 3 independent experiments done in triplicate). The EC_{50} and Hill coefficient were estimated as 84 ± 5 nM and 1.7 ± 0.2, respectively, from the regression curve of specific binding.

(C) Distribution of density of mGluR3 molecules on HEK293 cells in the single-molecule imaging analyzed in Fig. 2A, B (n = 400 cells). The number of particles in each cell was estimated from the results of SMT analysis of the first frame in each movie with negligible photobleaching.

(D) Specific and non-specific binding of SF650 ligands to HEK293 cells cultured in the same 96-well plates shown in **(B)**. Data are shown as mean ± SEM (n = 3 independent experiments done in triplicate). The EC_{50} and Hill coefficient was estimated as 21 ± 3 nM and 1.9 ± 0.4, respectively, from the regression curve of specific binding.

Fig. S3

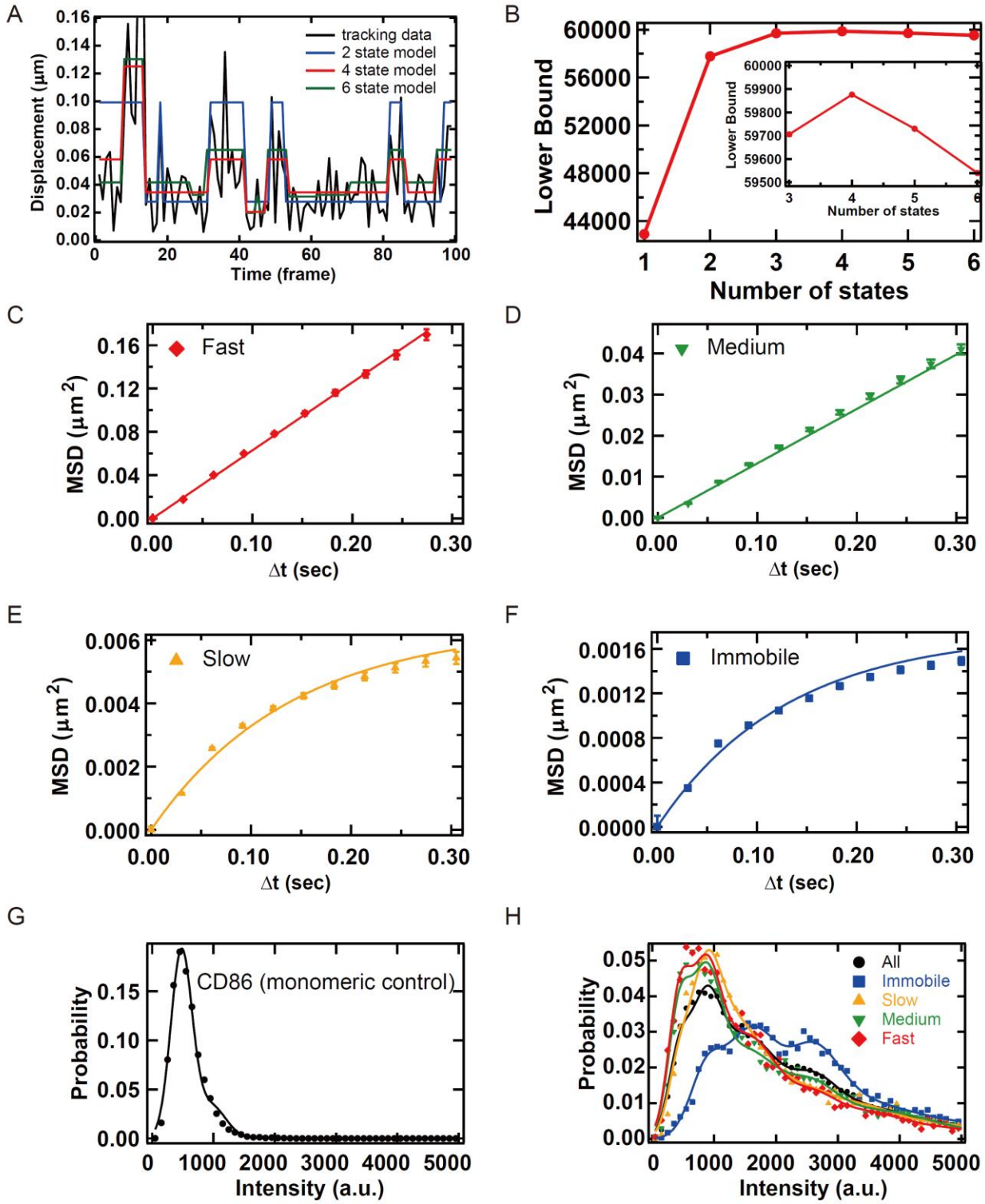
A
tracking data
2 state model
4 state model
6 state model
Displacement (μm)
Time (frame)
B
Lower Bound
Number of states
C
Fast
MSD (μm²)
Δt (sec)
D
Medium
MSD (μm²)
Δt (sec)
E
Slow
MSD (μm²)
Δt (sec)
F
Immobile
MSD (μm²)
Δt (sec)
G
CD86 (monomeric control)
Probability
Intensity (a.u.)
H
All
Immobile
Slow
Medium
Fast
Probability
Intensity (a.u.)

Fig. S3. Example of the VB-HMM analysis of mGluR3 trajectories

(A) Time series of the displacement of a particle within a frame (black line) clustered based on the two-, four-, and six-state models (blue, red, and green lines, respectively).

(B) Comparison of the likelihood of the clustering results with the different number of states. The highest lower bound L_q corresponds to the number of states with the maximum evidence obtained by the VB-HMM method (equation 30 in Methods). The inset shows the enlarged view from three to six states. The four-state model showed the highest lower bound.

(C-F) MSD-Δt plots of each diffusion state determined from the same cell in Fig. 3A, B. (C) Fast and (D) medium states show linear plots, indistinguishable from the free diffusion of particles. (E) Slow and (F) immobile states show concave plots, suggesting that the particles diffuse in a confined domain. Data are shown as mean ± SEM from 7760 (immobile), 5278 (slow), 7009 (medium), 4708 (fast) steps, respectively.

(G) Intensity histogram of TMR-labeled CD86 measured under the same conditions as mGluR3 as a monomeric control.

(H) Intensity histograms of TMR-labeled mGluR3 from the same cell in Fig. 3A, B. The data from immobile, slow, medium, fast, and the total trajectories are shown in blue, yellow, green, red, and black, respectively.

The histograms in (G, H) were fitted by the sum of Gaussian functions (equation 7 in Methods).

Fig. S4

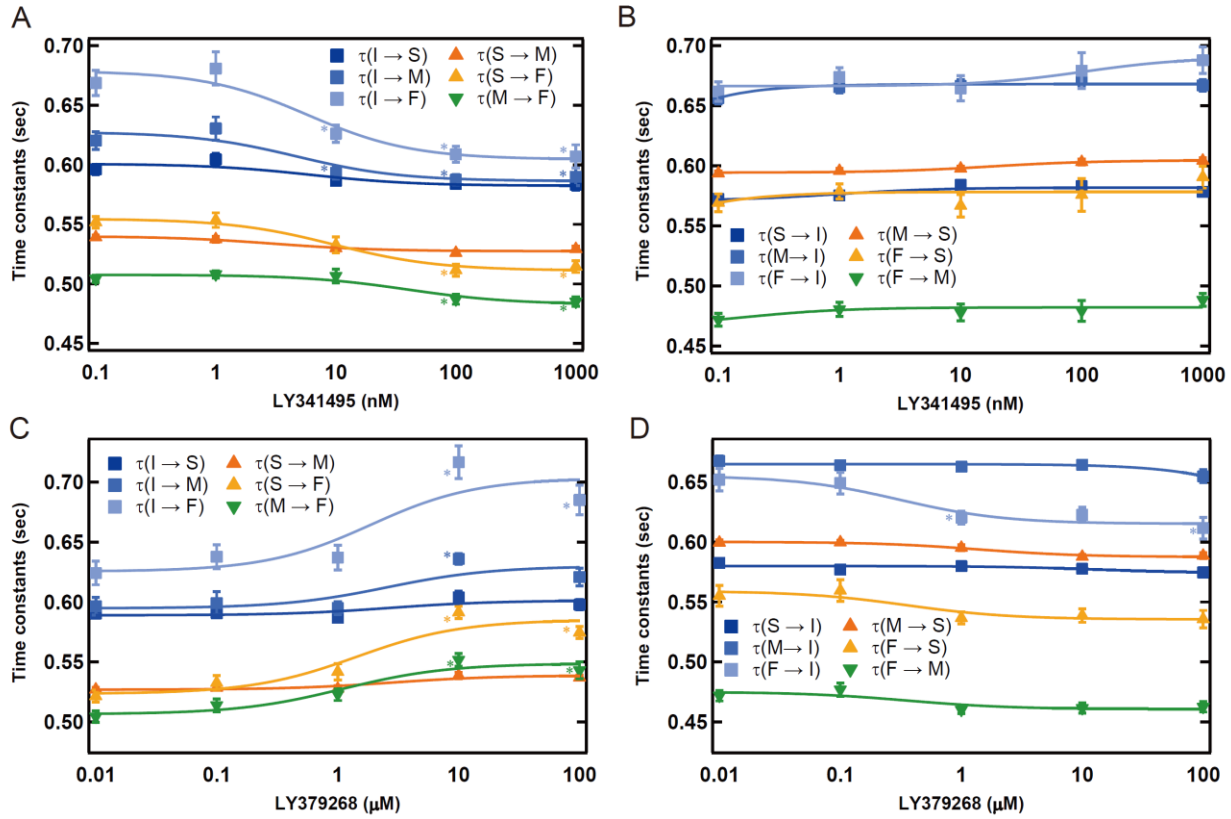

Fig. S4. Dose-dependent change in the time constants of the state transition
Time constants of the state transition are estimated from the transition probability within a frame (30.5 ms) of VB-HMM analysis. (A, B) LY341495 and (C, D) LY379268 dependencies for 100 nM LY314195. (A, C) Time constants of the transitions from slower to faster states. (B, D) Time constants of the reverse reaction. All the data are shown as mean ± SEM (n = 20 cells). * Significant difference in the time constants compared with the leftmost point in each curve (difference more than 3% and $p < 0.01$; t-test, two-tailed).

Fig. S5

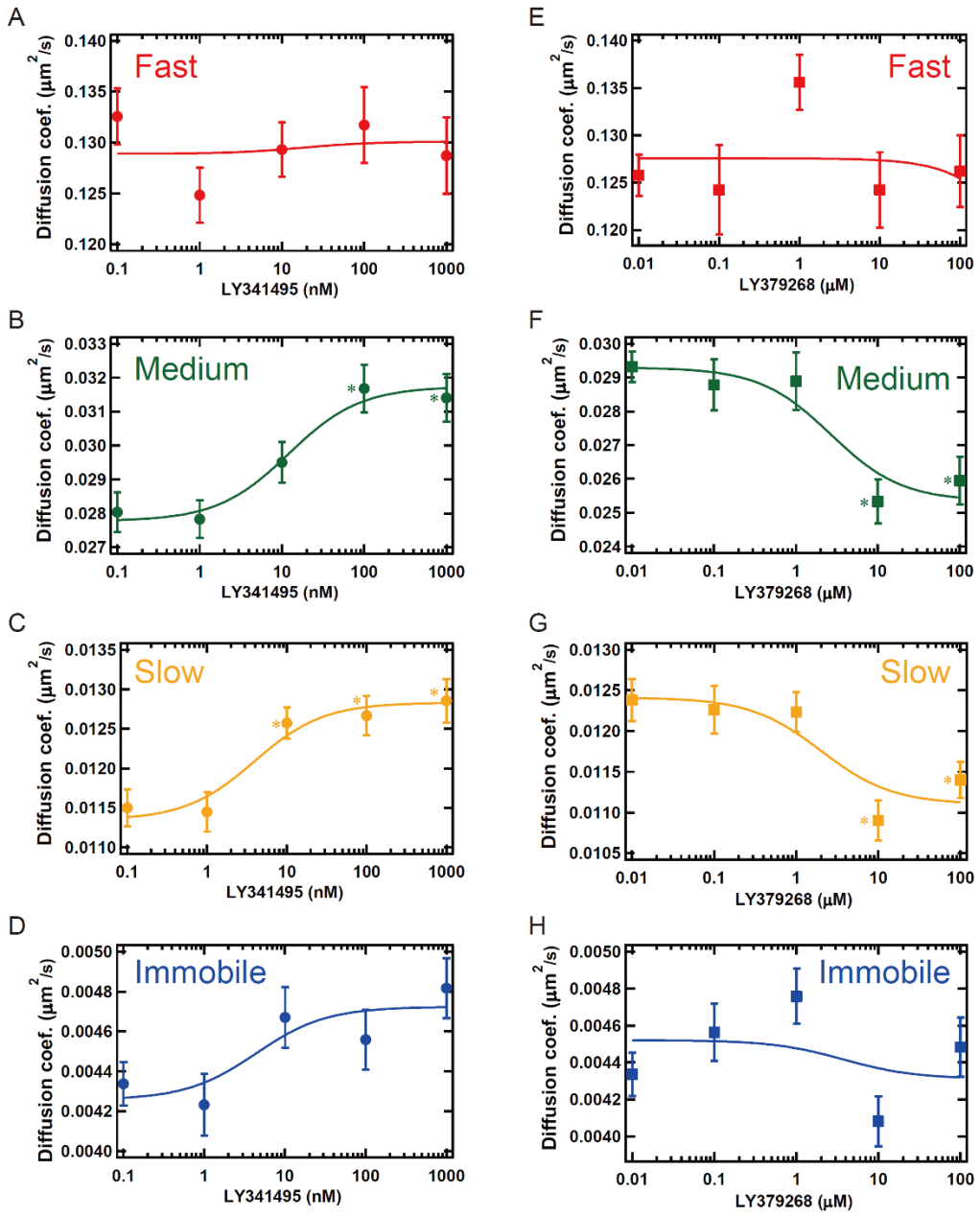

Fig. S5. Dose-dependent change in the diffusion coefficient of each diffusion state
Diffusion coefficient of each state was estimated from the step size within a frame (30.5 ms) by VB-HMM analysis. LY341495-dependency of the diffusion coefficients of (A) fast, (B) medium, (C) slow, and (D) immobile states. LY379268-dependency under 100 nM LY314195 of (E) fast, (F) medium, (G) slow, and (H) immobile states. * Significant difference in the diffusion coefficient compared with the leftmost point in each curve ($p < 0.01$; t-test, two-tailed).

Fig. S6

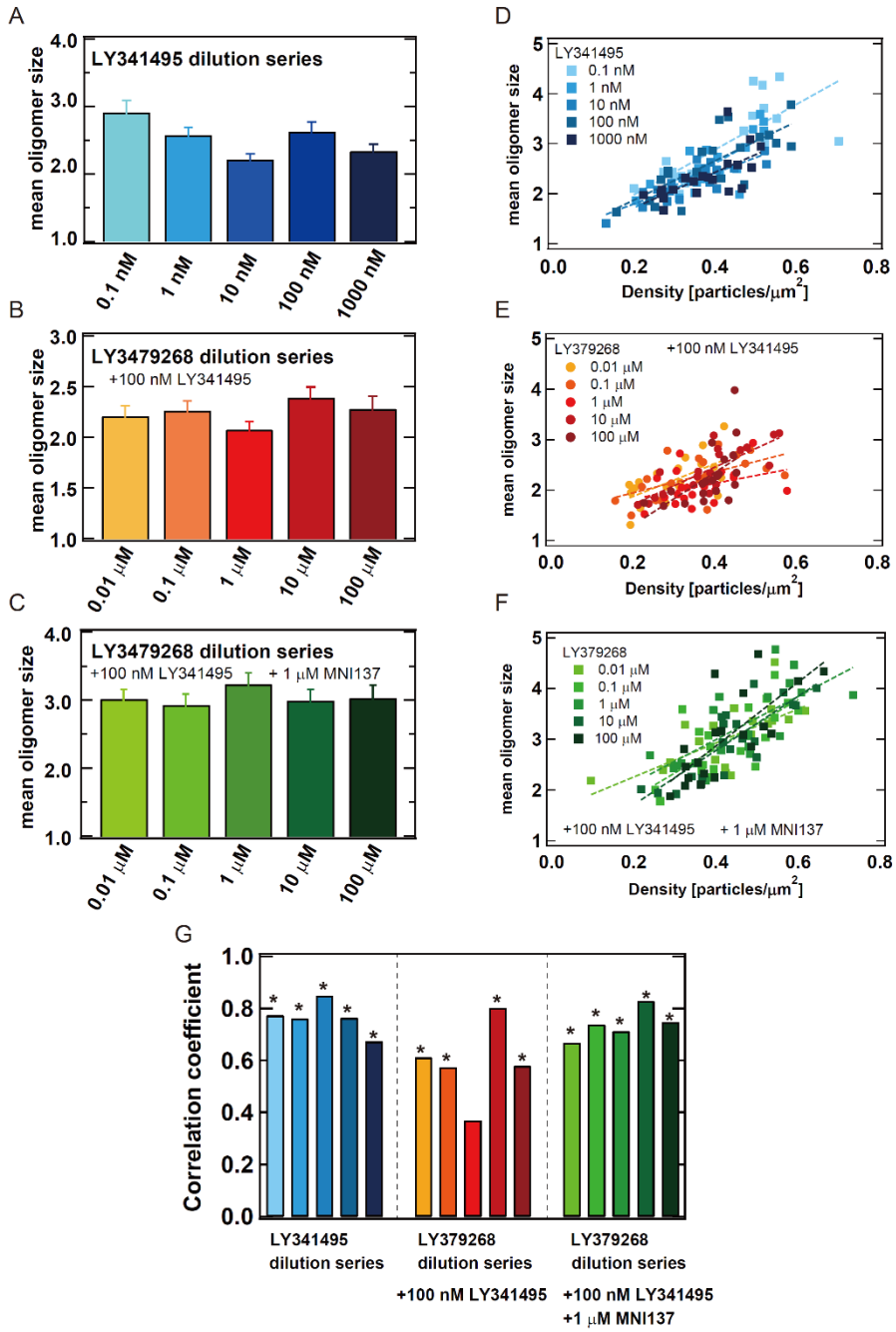

Fig. S6. Correlation between mean oligomer size and receptor density in various ligand conditions

(A-C) Mean oligomer size of mGluR3 on the HEK293 cell surface under various ligand conditions. The mean oligomer size in each cell was estimated from the intensity histogram of the same cells analyzed in Fig. 1C–E, based on the sum of Gaussian functions (equations 7 and 8 in Methods). Data are shown as mean ± SEM (n = 20 cells). (D–F) Correlation between mean oligomer size and receptor density. Each point shows a single cell. The dashed lines are regression lines. (G) Pearson's correlation coefficients estimated from the data in (D-F). * Significant correlation between mean oligomer size and receptor density ($p < 0.01$; n = 20 cells).

Fig. S7

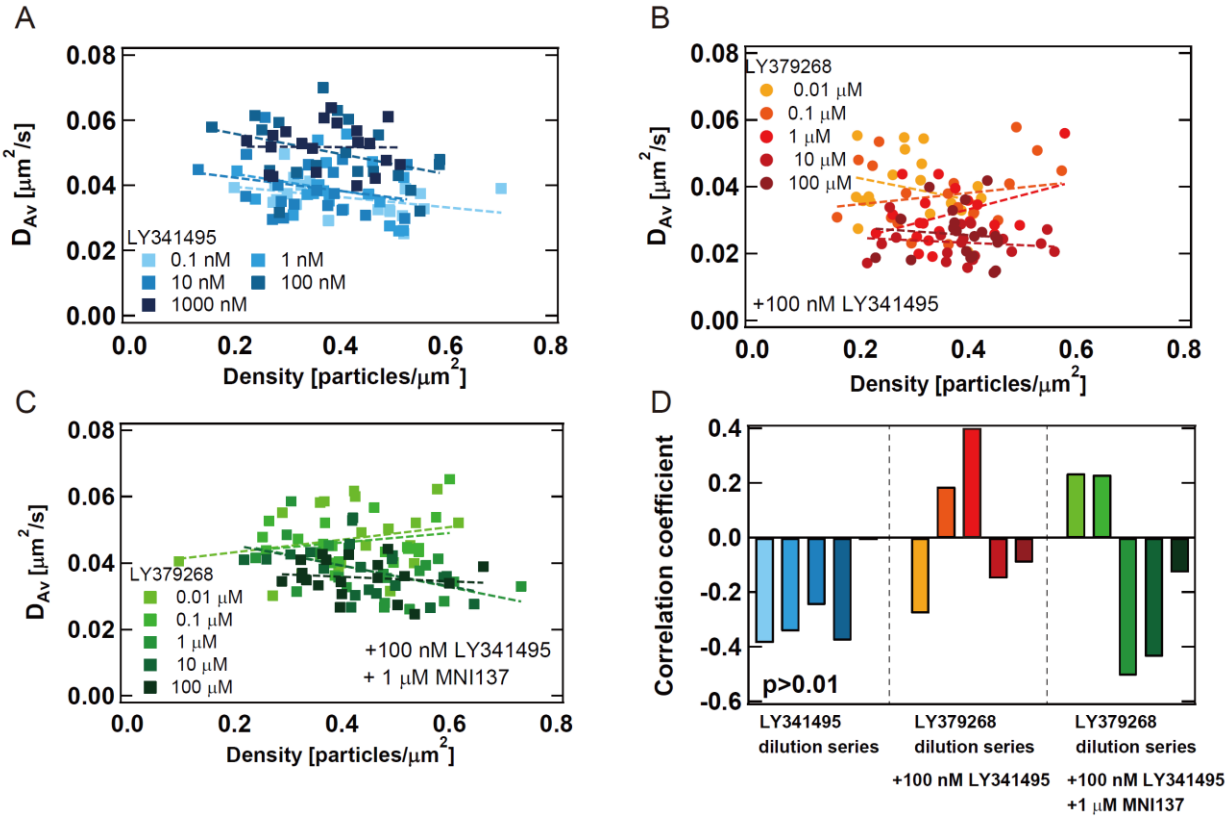

Fig. S7: Correlation between D_{Av} and receptor density in various ligand conditions
(A-C) Correlation between D_{Av} and receptor density of the same cells analyzed in Fig. 1C–E. Each point shows a single cell. The dashed lines are regression lines. (D) Pearson's correlation coefficients estimated from the data in (A–C). D_{Av} was not significantly correlated with receptor density ($p > 0.01$; $n = 20$ cells).

Fig. S8

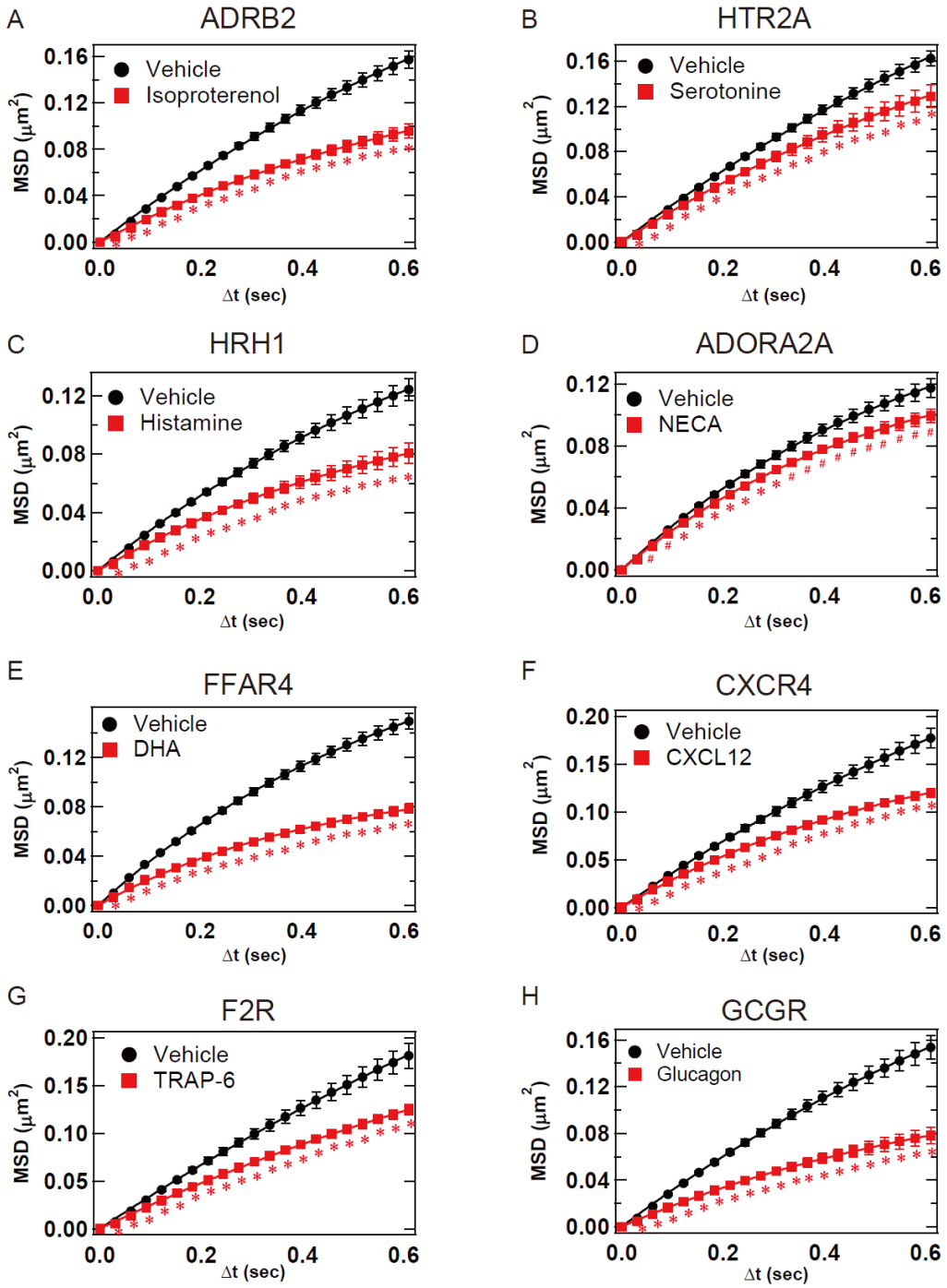

Fig. S8. MSD-Δt plots of the trajectories of GPCRs with or without agonist
MSD-Δt plots of the trajectories of STELLA Fluo 650-labeled (A) ADRB2, (B) HTR2A, (C) HRH1, (D) ADORA2A, (E) FFAR4, (F) CXCR4, (G) F2R, (H) GCGR on living HEK293 cell surface with (red square) or without (black circle) agonist stimulation. All the data are shown as mean ± SEM (n = 20 cells). *, # Significant difference in MSD at each Δt (p < 0.01 and p < 0.03, respectively; t-test, two-tailed).

Supplemental Movie legends

Movie 1. TIRFM of TMR-labeled mGluR3 molecules on a HEK293 cell
Movements of TMR-labeled mGluR3 molecules on a HEK293 cell without ligands are monitored by TIRFM (Methods). The playback speed of the movie is 33 fps (real time). Left panel shows a whole cell image, and right panel shows an enlarged view of the dashed square in the left panel (3–12 s). The trajectories of mGluR3 molecules are shown as yellow lines in the right panel (6–9 s). The trajectories are divided into four diffusion states by the VB-HMM analysis (9–12 s).

Movie 2. Accumulation of mGluR3 molecules followed by disappearance with rapid movement
Accumulation and disappearance of mGluR3 on a HEK293 cell without a ligand are monitored by TIRFM (Methods). The playback speed of the movie is 164 fps (5× speed). Left panel shows a whole cell image, and right panel shows an enlarged view of the dashed square in the left panel.

Movie 3. Dual-color TIRFM of TMR-labeled mGluR3 and GFP-labeled CLC
Colocalization between TMR-labeled mGluR3 (red) and GFP-labeled CLC (green) on a HEK293 cell with 100 μM LY379268 is monitored by dual-color TIRFM (Methods). The size of image is 100 × 100 pixels (67 nm/pixel). The playback speed of the movie is 164 fps (5× speed). The green channel (Gch), red channel (Rch), and merged image movies are shown in the left, middle, and right panels, respectively. The merged particles are shown in yellow.

Movie 4. TIRFM of various GPCR molecules on a HEK293 cell with and without agonist
Movements of STELLA Fluo 650-labeled ADRB2, HTR2A, HRH1, ADORA2A, FFAR4, CXCR4, F2R, and GCGR molecules on a HEK293 cell with and without agonist are monitored by TIRFM (Methods). The playback speed of the movie is 33 fps (real time). Left panel shows the vehicle conditions, and the right panel shows agonist-stimulated conditions.